Simulation, Design and Test of Brushless, Self-Excited Synchronous Field-Winding Machine

by

Abdurazak Zeynu Mohammed

A dissertation submitted in partial fulfillment
of the requirements for the degree of
Doctor of Philosophy
(Electrical Engineering: Systems)
in The University of Michigan
2017

Doctoral Committee:

Professor Heath F. Hofmann, Chair
Professor Ian A. Hiskens
Professor Jessy W. Grizzle
Professor Bogdan I. Epureanu

Abdurazak Zeynu Mohammed

mzeynu@umich.edu

ORCID iD: 0000-0002-4160-4519

To my mom, for your selfless love and care.

And To Yoni, Andy and Beck for all your support and for being such amazing brothers!

ACKNOWLEDGEMENTS

I would like to begin by expressing my heartfelt gratitude and thanks to my advisor professor Heath Hofmann, for his guidance, support and valuable advice through out the project. His humble and helpful personality makes it easy for me to learn from his knowledge and insights in the field. In addition to the research work, the courses I took with him, my work as GSI, the summer Electrify Tech camp, and the voluntary summer course he gave at Addis Ababa Institute of Technology (AAIT) in 2015, gave me more chance to work with him and I have got a great deal of learning and experience, both academic and hands-on. I am grateful to all of that and have always been happy to have him as my PhD advisor!

I would also like to express my gratitude and thanks to professor Ian Hiskens. Since my first semester at Michigan, I have benefited from his knowledge and wisdom. Besides the academic related advise, professor Hiskens has been someone I go to, even when I am stressed or frustrated, and always taking time, giving me good counsel. I am grateful and really appreciate it!

I would also like to express my gratitude and thanks to professor Jessy Grizzle for his positive, encouraging comments and attitude during all my encounter with him since my first qualifying exam; to professor Bogdan Epureanu for accepting my request to be a cognate member and always being flexible in scheduling, and to all committee members in general for giving your time and effort to serve in my thesis committee.

In addition, I would like to say thank you to Memhr Solomon Bekele for making

math fun at early stage of my school year and to Memhr Tamru at Tikur Anbessa High School for instilling in us the view of learning science to appreciate nature, to Memhr Alemu at Bahir Dar University for teaching physics with applications in a way we enjoy it.

I like to express my sincere gratitude to Becky (Becky Turanski), Shelly(Michele Feldkamp), Judi Jones, Jose (Jose-Antonio Rubio), for their advice and for taking care of office and purchasing processes. There were times that I needed parts the next day for experiment to continue, and Shelly always go extra mile to make that happen, I really appreciate that and thank you! My special thanks to Kent Prus of the Auto Lab, for being unceasingly helpful in machining and modifications of different parts during the prototype building, as well as when modifications are needed during test.

I really appreciate the help from my labmates Prerit Terway, Jason Pries, Jun Hou, David Reed, Kan Zhou, Victoria Chung, and Yuanying Wang in collecting data and making the experiments setup up, thank you all! I would also like to say thank you to Fanny Pinto Delgado, for all the time spent in the lab with me, helping with the latest data collection, and also while fixing or changing test setups. I really appreciate all in our group for being such friendly and helpful partners.

I would also like to express my gratitude to Aaron Stein, Mads Almassalkhi, Hamid Ossareh, Patricia Laskowsky, Soumya Kundu for being good friends that make my time at Michigan enjoyable, to Hector Palacious for being such listener and caring friend, and to all of Saint Abune Teklehaymanot church community for making me feel like home.

Above all thanks to Almighty God!

እግዚአብሔር ይመስገን!

TABLE OF CONTENTS

LIST OF FIGURES

Figure

LIST OF TABLES

Table

ABSTRACT

The high cost of rare-earth materials has spurred interest in the development of high-performance electric machines which do not require these materials. However, other conventional machine architectures suffer from relatively low efficiency and power density when compared to rare-earth permanent-magnet machines. Synchronous field-winding machines have performance characteristics similar to those of rare-earth magnet machines. However, the power density and cost of conventional field-winding machines are adversely affected by the mechanisms which convey power to the field windings. This thesis presents a brushless, self-excited synchronous field-winding machine design. The rotor of this machine possesses two windings, a field winding and a transformer winding, that are connected through a diode rectifier circuit. Using field-oriented control techniques, an AC magnetic field is generated by the stator windings that is always aligned with the transformer winding. A simulation model which combines a finite element model of the machines magnetic behavior with a nonlinear circuit model of the diode rectifier is developed and used to design the machine. Experimental results from a prototype machine are presented.

CHAPTER I

Introduction

1.1 Review on Relevant Concepts and Theories

1.1.1 On Electric Drives

The importance of electric drives is easily appreciated when we observe their application in almost every aspect of our daily lives. These applications range from pumps, heating systems, robotics, CD players, drones, toys, vehicle propulsion, and many more. Making use of different motor types, electric drives constitute one of the major components of the modern industry. In industrialized countries, more than 40% of generated electrical energy is used in motor drives [14][7].

High-performance variable speed applications today require advanced control[5] [12] to achieve precise position, speed, torque or power. These control techniques have been evolving since 1896, when Harry Ward Leonard introduced his solution to a variable speed DC drive, [14]. Presently we have more sophisticated controls, using microcontrollers. Field-Oriented Control (FOC) is the most popular technique used in high-performance AC motor control applications (§ 1.1.1.3).

Figure 1.1 shows a typical drive system represented by a simplified block diagram, showing the key components of the system that are described below.

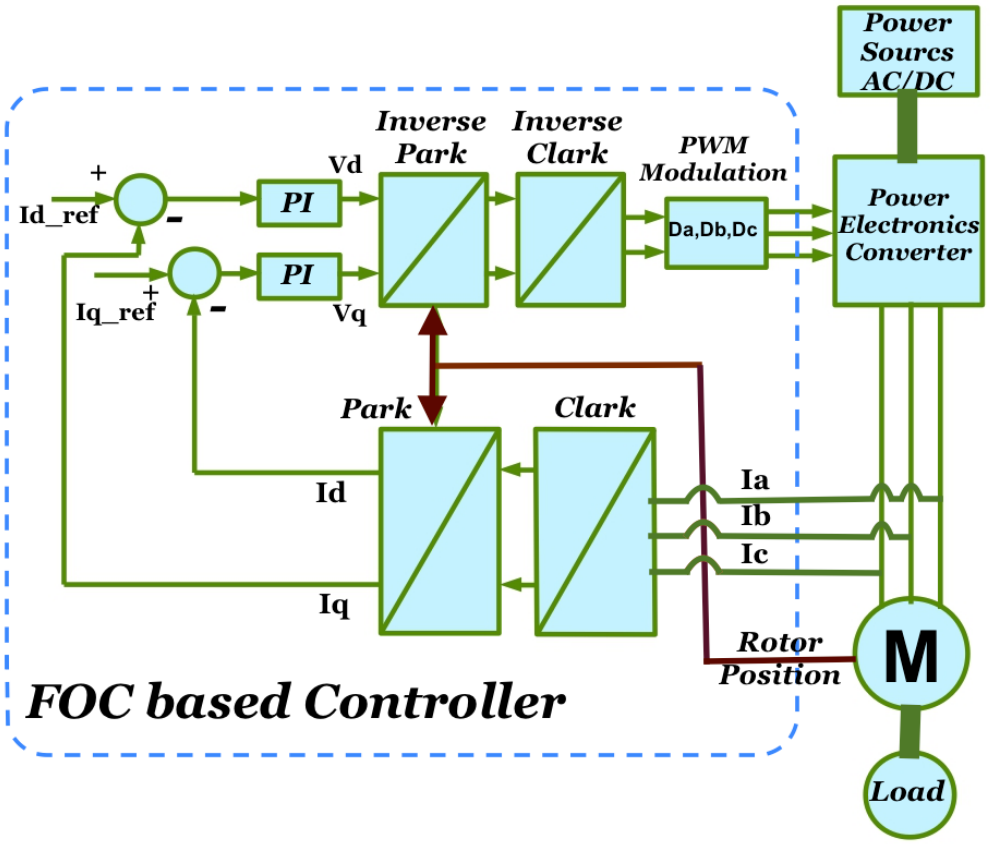

Figure 1.1: Basic components of electric drive system

Controller: Modern controllers are typically implemented on digital signal processors (DSPs) or microcontrollers, and high-level embedded platforms are also available in the market with the capability of hardware-in-the-loop features that facilitate the development and testing of control algorithms. The controller implements the specific control algorithm using feedback from sensors, and sends commands to the power electronic converter so that appropriate voltages or currents are supplied to the machine[9][45][43].

Power Electronic Converter: These converters contain a set of power electronic switches that are controlled to convert and transfer power between the main power source and the motor. The type of converter depends on the machine and control technique implemented. MOSFETs and IGBTs are the most commonly used power

electronic switching devices in drive system applications today. Converters also have what is called gate-drive circuitry that interfaces the controller with the switching devices[32].

Electric Machines (M): A variety of machine types: direct current (DC) machines, induction machines, synchronous machines, variable reluctance machines, and stepper motors, are among the most commonly used. The selection of the specific machine depends on the application load profile and other constraints like cost and space. Each machine topology has its own unique advantages that make it appropriate for different applications.[4]

Power Source: Some machines, like induction machines, have applications where they are directly driven from the AC utility voltages. However, in such cases, there isn't much control; it is either in the ON or OFF state, with the possibility of transients at the start and stop. For high-performance, variable-speed applications, however, it is common to use DC voltages as the main power source, and a power electronic converter to generate appropriate voltages to the machines.

Load: The load represents the specific mechanical requirements(i.e. torque, speed) of the application. This dictates the choice of the machine to use, the sensors to use, and also the type of control to implement.

Sensors: Sensors are to be mounted on the load, the machine, or the inverter to measure speed, position, current, and voltage, for control as well as for protection.

Desired characteristics of electric drives include, but are not limited to: large power capability, full torque at stand-still, a wide speed range, environmentally clean

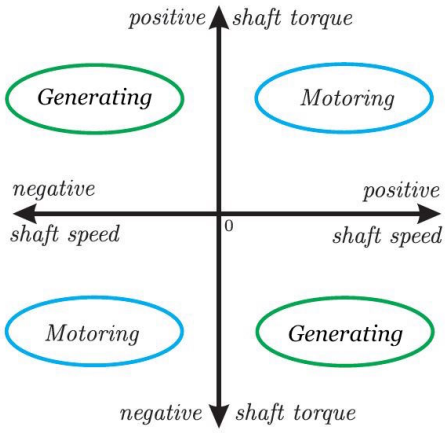

Figure 1.2: Four-quadrant operation [2]

and safe operation, minimal maintenance requirements, minimal audible noise, and four-quadrant operation, as shown in Figure 1.2, where the machine is capable of motoring and generating modes in either direction of rotation.

1.1.1.1 Two-phase, D-Q Model of Three-phase AC Machines

The most popular AC machine used with drives today are of three-phase design. In the control design of three phase AC machine drives, the Stanley dynamic model [18] is commonly used due to its advantages in the analysis of these machines as well as in the development of their controls, particularly with high-performance vector control techniques[15][16]. This is achieved by converting the three-phase machine design into an equivalent two-phase model. This also leads to the modeling of the electric variables of the machine with two-dimensional vectors which rotate at a constant angular velocity under steady-state operation, imposing a rotating magnetic field on the rotor of the machine [18].

This modeling is explained using a cross-section of the two-phase two-pole, AC stator, shown in Figure 1.3. It is called a two-pole stator because the magnetic field generated by the stator windings and imposed on the rotor has two poles, one north (entering the rotor) and one south. This model is particularly useful for control

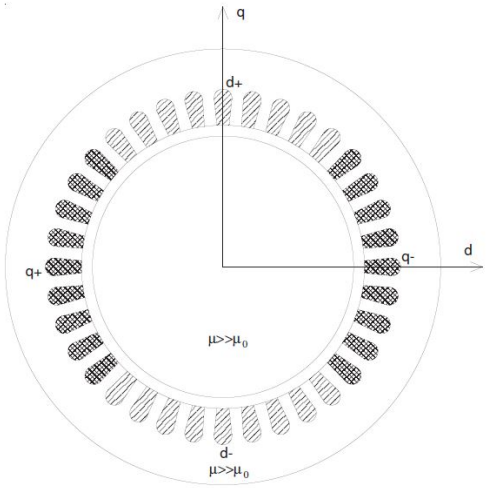

Figure 1.3: Two-phase stator model [18]

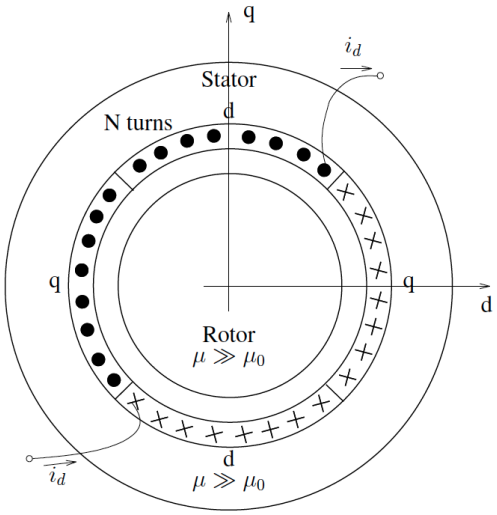

Figure 1.4: Smooth airgap, two-phase model including the rotor [18]

purposes. The smooth-airgap model neglects the effects of ripple in the torque due to the slots in the stator iron and the winding structure, yet reliably captures the fundamental behavior of the machine.

Applying the right-hand rule reveals that a positive current flowing in the direct winding will generate a magnetic field in the rotor whose direction is aligned with the direct axis (d), and positive current flowing in the quadrature winding will generate a magnetic field in the rotor aligned with the quadrature axis(q). By commanding currents i_d and i_q simultaneously, the two-phase, two-pole AC stator can impose a magnetic field of arbitrary magnitude and direction on the rotor, [18].

1.1.1.2 Reference Frames and Reference Frame transformation

The directions of the d and q-axis magnetic fields generated by the stator windings of the two-phase machine correspond to the axes of a Cartesian coordinate system. This also provides a physical frame of reference for the two-phase stator current vectors, i_d and i_q, and is called the ***stationary reference frame***, as it is associated with the stator [18].

In the analysis of AC synchronous machines, it is common to use a reference frame that is aligned with the rotor structure rather than with the stator structure, and hence it is called the ***synchronous reference frame***, as these reference frames rotate in synchronism with the two-phase vectors in steady state.

The synchronous reference frame is useful in that the vectors associated with the two-phase electrical variables of the machine are constant in the synchronous reference frame. In both analysis and control it is easier to work with constant, rather than time-varying, variables.

The following are mathematical tools that are used for reference frame transformations and give the ability to transform variables from one reference frame to another, as desired, in the analysis or control of electric machines.

- 90^o **rotation matrix, counterclockwise (CCW)**

  Figure 1.5 shows a 90^o rotation of vector $\vec{x}$,

  where $\mathbf{J} = \begin{bmatrix} 0 & -1 \\ 1 & 0 \end{bmatrix}$.

  This matrix is analogous to the imaginary number j, which accomplishes the same effect in the complex plane.

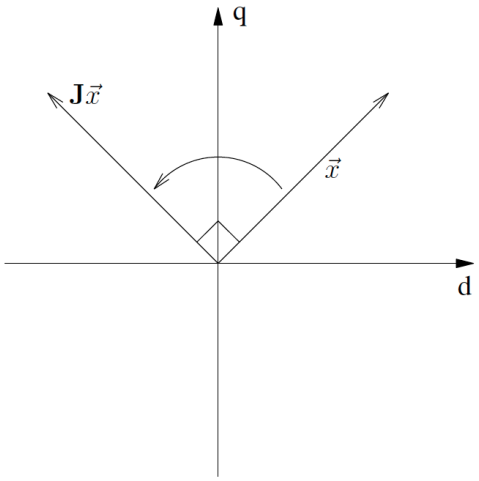

Figure 1.5: 90^o vector rotation [18]

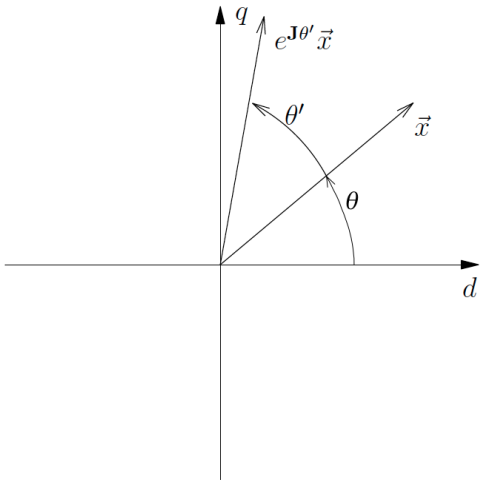

Figure 1.6: Arbitrary angle vector rotation [18]

- **Arbitrary angle rotation matrix**

  Figure 1.6 shows the transformation to rotate the vector $\vec{x}$ by an arbitrary angle θ' in the counterclockwise direction. The resulting vector will have angle of $\theta+\theta'$ and its direct and quadrature axis components can be expressed as, [18]

$$x'_d = x_d cos(\theta') - x_q sin(\theta') \tag{1.1}$$

$$x'_q = x_q cos(\theta') + x_d sin(\theta') \tag{1.2}$$

  this can also be expressed in matrix form as:

$$\vec{x'} = e^{\mathbf{J}\theta'}\vec{x} \tag{1.3}$$

  where,

$$e^{\mathbf{J}\theta'} = \begin{bmatrix} cos(\theta') & -sin(\theta') \\ sin(\theta') & cos(\theta') \end{bmatrix}$$

- **Clark Transform, (abc-dq)**

  This transform converts three-phase variables to corresponding equivalent two-phase values in the stationary reference frame. Figure 1.7 shows the three-phase (left) and two-phase (right) models of the machine in the stationary reference frame. In principle, the two models have the same basic operation, and so it is possible to develop an equivalent two-phase model of a three-phase AC stator, a model which would impose the same rotating magnetic field on the rotor.

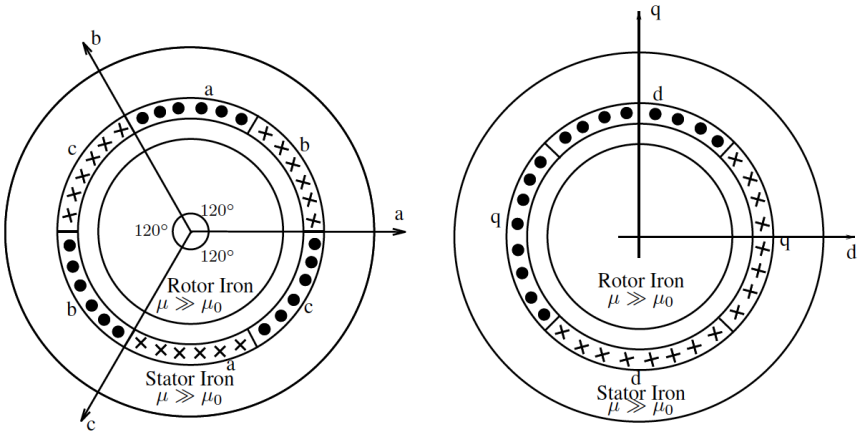

Figure 1.7: Two-pole, smooth-airgap AC stators. Left: three-phase stator. Right: two-phase stator-quadrant operation [18]

Our control implementations require us to convert the measured three-phase electrical variables into their equivalent two-phase values for the control algorithm, and then convert the two-phase output commands of the controller into their equivalent three-phase values. This is achieved using the Clark transform, [18]:

$$x_d = \frac{2}{3}x_a - \frac{1}{3}x_b - \frac{1}{3}x_c \tag{1.4}$$

$$x_q = \frac{\sqrt{3}}{3}(x_b - x_c) \tag{1.5}$$

The "zero-sequence" current, which consists of the average of the three-phase variables, is given by:

$$x_0 = \frac{1}{3}(x_a + x_b + x_c) \tag{1.6}$$

The Clark transform, can be written in vector form as follows:

$$\begin{bmatrix} x_d \\ x_q \\ x_0 \end{bmatrix} = T_{23} \begin{bmatrix} x_a \\ x_b \\ x_c \end{bmatrix} \tag{1.7}$$

where

$$T_{23} = \begin{bmatrix} \frac{2}{3} & -\frac{1}{3} & -\frac{1}{3} \\ 0 & \frac{\sqrt{3}}{3} & -\frac{\sqrt{3}}{3} \\ \frac{1}{3} & \frac{1}{3} & \frac{1}{3} \end{bmatrix}$$

The corresponding inverse transform is accomplished using the matrix:

$$\begin{bmatrix} x_a \\ x_b \\ x_c \end{bmatrix} = T_{32} \begin{bmatrix} x_d \\ x_q \\ x_0 \end{bmatrix}, \tag{1.8}$$

where

$$T_{32} = \begin{bmatrix} 1 & 0 & 1 \\ -\frac{1}{2} & \frac{\sqrt{3}}{2} & 1 \\ -\frac{1}{2} & -\frac{\sqrt{3}}{2} & 1 \end{bmatrix}$$

- **The Park Transform**

  The Park transform is used to determine the direct and quadrature components of a given vector $\vec{x}$ with respect to a new coordinate system associated with a synchronous reference frame, designated by a superscript "**syn**". One property of such a reference frame transformation is that the magnitude of the vector will be unchanged in the new reference frame. From [18], the Park transform can be implemented using the equations:

$$x_d^{syn} = cos(\theta_{syn})x_d + sin(\theta_{syn})x_q \tag{1.9}$$

$$x_q^{syn} = -sin(\theta_{syn})x_d + cos(\theta_{syn})x_q \tag{1.10}$$

  And the corresponding inverse transform is given as:

$$x_d = cos(\theta_{syn})x_d^{syn} - sin(\theta_{syn})x_q^{syn} \tag{1.11}$$

$$x_q = sin(\theta_{syn})x_d^{syn} + cos(\theta_{syn})x_q^{syn} \tag{1.12}$$

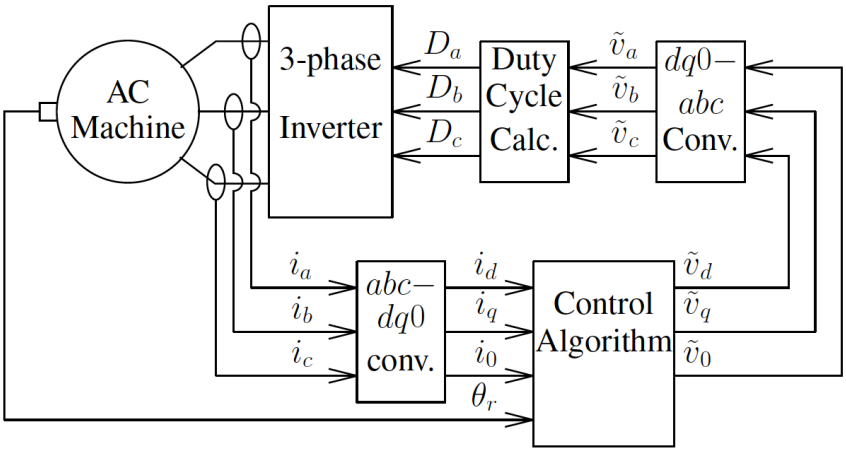

Figure 1.8: High-performance controller using dq0 model of machine [18]

1.1.1.3 Field Oriented Control

Field-Oriented Control (FOC)[38][35] consists of regulating the stator currents in a synchronous reference frame, and is the most popular high-performance control scheme for AC drives today. It is based on two-phase machine models; therefore, in the implementation of this control algorithm, one must convert the measured three-phase electrical variables into their equivalent two-phase values, and later convert back the two-phase output commands of the controller into appropriate three-phase values.

Figure 1.8 shows a block diagram depiction of the FOC algorithm. It involves current feedback from sensors, applying transformations, and also makes use of feedback control to regulate the desired output. Microcontrollers are commonly used in such applications, as implementation involves significant computations[18][22].

1.1.2 On Electric Machines

1.1.2.1 Energy Conversion Devices

As the basic principle of energy conversion states, energy is transformed from one form to another, it is neither created nor destroyed. An electric machine can be described as an apparatus that converts electrical energy to mechanical energy when operating as a motor, or mechanical energy to electrical energy when operating as a generator, as shown in Figure 1.9 . The majority of electric machines can run either as a motor or generator depending on the mode of operation.

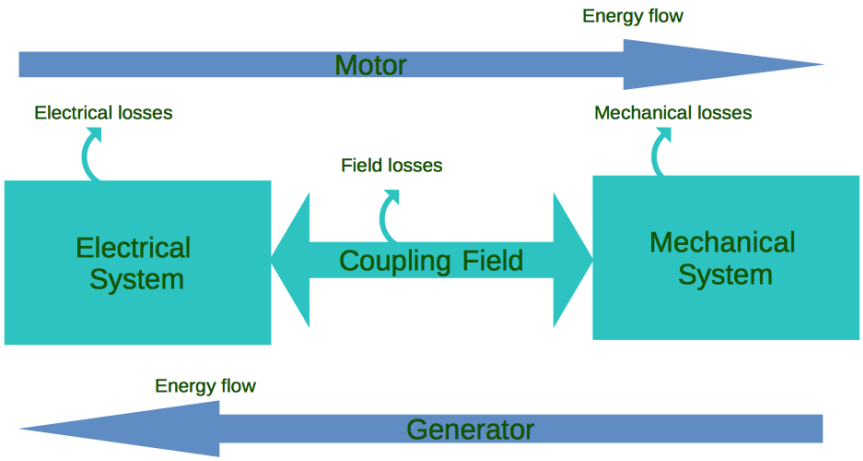

Figure 1.9: Schematic showing the energy conversion [2]

The electrical power can be quantified in terms of the currents and voltages at the terminals of the machine. Mechanical power is manifested in the form of a linear or translational motion, rotation, or any other motion type depending on the application. There are different machine topologies, which vary in their constituting components, in how these components move with respect to each other, and/or also in how the components are assembled.

Considering the relevance to this research work, we will be focusing on the most common rotary-type machines. Typically, these machine types consist of two main components: a stationary component referred to as **stator**, and a rotating part,

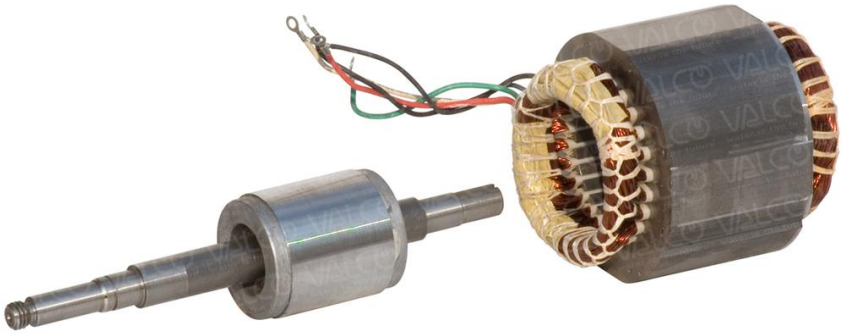

Figure 1.10: Rotor and stator structure [40]

referred to as a **rotor**. Figure 1.10 shows a representative picture of rotor and stator structures.

The rotor is usually contained inside the stator, separated by an air gap, and held in place by a shaft usually with bearings at both ends. A shaft is also typically used to couple the machine with the external mechanical load.

In most applications, the stator and rotor are made of electrical steel with a high magetic permeability that maximizes the magnetic coupling between the stator and rotor, and increases the stored magnetic energy. The steel also helps shape and distribute the magnetic fields as required by the design. These steel structures are typically made of thin laminations to help minimize eddy-current losses. Depending on the machine type, the magnetic flux required for its operation is produced using either current-carrying windings or permanent magnets.

Energy conversion occurs through the interaction of magnetic fields when changes in the magnetic flux-linkage result from mechanical motion. Voltages are induced in windings by creating relative motion between the windings and a magnetic field.

In the case of a motor, electrical energy is supplied to the windings of the stator, and electromagnetic interaction with the rotor produces torque, and hence mechanical energy output, in the form of rotation of a shaft. In the case of a generator, a rotary

motion is provided by a prime mover acting on the rotor to provide the mechanical energy, and the relative motion between the magnetic field and the conductors generates the electrical energy output.

1.1.2.2 Evolution of Electric Machines and Major Topologies

Electric machines came into existence in the 19^{th} century, and most of the topologies actively used today were invented at this early stage in the era of electricity.

The exception to this is permanent magnet machines, which showed substantial progress around the end of the 1930s. Helped by advances in power electronics and control technology [39],[9] PM machines kept increasing their number of applications and their power levels. Figure 1.11 shows the evolution of brushless machines from the "classical" machines:

- DC commutator/with wound field,
- AC synchronous, and
- AC induction.

The term "classical" refers to their commonality in producing constant torque, and their ability to operate from or produce pure DC or AC sinewave voltages. They can also readily be used in variable-speed applications using power electronic inverters. This makes them applicable in fixed-speed as well as in variable-speed applications, [39]. The other machine topologies are derived from the classical ones, replacing the field windings either with permanent magnets or changing their configurations.

Considering only AC machines, as they are directly related to the research topic, one can easily notice from Figure 1.11 that they all have a 3-phase AC stator that is essentially the same. In the case of PM brushless DC machines, it is a concentric 3-phase winding, whereas in the others it is optimally distributed winding to produce

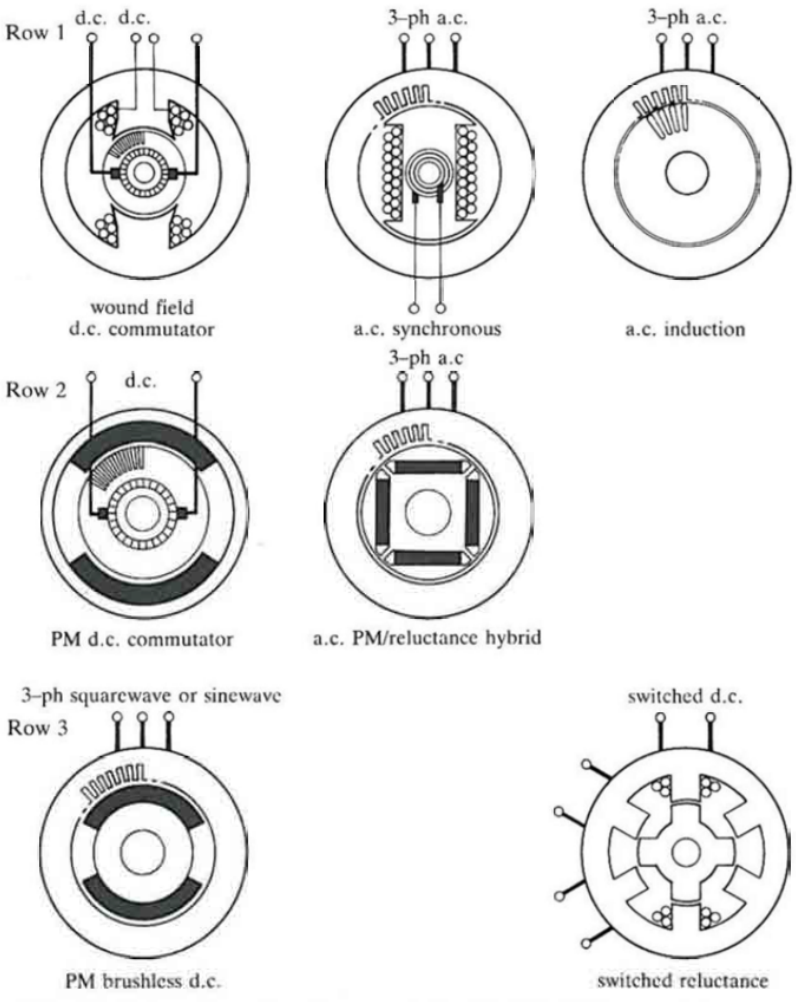

Figure 1.11: Evolution of electric machines [39]

flux with close to sinusoidal waveforms. So it can be asserted that the major difference among most AC machines lies in the mechanism of **how the rotor field is generated**.

The derived topologies are mostly used in specialty applications, and recent developments have increased their use at higher power ratings, such as the use of PM synchronous machines in wind power generators, electric vehicles, and hybrid electric vehicles.

1.1.2.3 Desired Performance Characteristics of Eletric Machines

Technological advances in different application areas like aerospace, military, robotics, and automotive industries have led to increased demand for high-performance drives, and hence increased demand for high-performance electric machines as well. Such levels of performance require these machines to have reduced losses, reduced weight and volume, as well as the capability of operating over a wide speed range.

Increased **power density** is an important characteristic desired in all kinds of applications, ranging from EVs where weight is directly related to the battery life to small robotics applications.

Improved **efficiency** as well as reduced **cost** directly relate to the economic aspects for end consumers. The latest global initiatives on reducing carbon emissions and the stringent regulations that come with them emphasize the need for much improved efficiency in these machines. In developed economies, $\frac{2}{3}$ of the primary energy converted to electricity is reconverted into mechanical energy in electric motors and drives [39], and this further emphasizes the need for higher efficiency.

Another important characteristic for electric machines that makes them preferable in a variety of applications is to have the capability of **constant power over a wide speed range, (CPWSR)**, where the machines are capable of providing a constant power level at any speed above the base speed of the machine, [2]. High-performance machines for aerospace applications typically drive high-speed compressors, fans, pumps, and actuators. The operating speeds of these applications cover a broad range, from 10 to 200 krpm [39], making the CPWSR feature particularly important for such applications.

1.1.2.4 Pros and Cons of The Major Topologies

The AC induction machine

Induction machines have a simple and relatively low cost construction [4]. They can be driven directly from a fixed-frequency voltage source. Using advanced drives, they can also be used in variable-speed applications, and can operate over a wide speed range [14]. Induction machines, however, suffer from relatively low power density, and poor power factor [39].

Synchronous Reluctance Machine

Synchronous reluctance machines can be used in variable speed applications [14]. They can run at high speeds due to the ease of controlling the stator flux-linkage, although their power output decreases with speed at high speeds [18]. There is no conduction loss in the rotor, which helps the efficiency of these machines, and they have comparable performance to that of induction machines. However, similar to the induction machines, they suffer from relatively low power density, poor power factor, as well as higher manufacturing cost [23] [12],[17].

Synchronous Machines, (PM and Field-winding)

In conventional synchronous machines, the three-phase stator generates a rotating magnetic field. Magnetic fields produced by the rotor lock to this field and they spin together in synchronism, hence the name synchronous. These machines spin at the same speed of the rotating field, independent of load variations.

These machines can have permanent magnets or DC electromagnets to produce the rotor magnetic poles. The PM-based machines provide fixed magnetic flux, whereas the DC electromagnets have adjustable rotor flux, which provides an additional degree of control for the machine. The DC current adds to the I^2R losses that dissipates as heat. On the other hand, the DC field winding machines need a DC source to supply the field currents. This is conventionally supplied by an external circuit in the stationary frame, making the contact with the rotor through slip rings and brushes

[4] [12].

Synchronous PM and field-winding machines are also both capable of achieving unity power factor, unlike induction and reluctance machines where a maximum power factor of 0.8 is common [18]. In variable-speed drive (VSD) applications, unity power factor means that the VSD can provide its peak power capability (based upon its voltage and current constraints) to the machine. For a given power rating of the machine, this can result in a reduced cost of the VSD, as transistors with lower current and/or voltage ratings can be used.

Synchronous field-winding, and certain permanent magnet machines, are capable of achieving CPWSR [39].

The PM and field-winding machines differ from induction and reluctance machines in that the rotor of the machine has an independent magnetic excitation, which allows them to have higher torque densities.

1.2 Motivation and State of The Art

Electric machines used in variable-speed drive applications, such as the propulsion of hybrid electric vehicles, must possess high efficiency, high power density, and low cost [18]. As discussed in the previous section, the major electric machine topologies have their own merits with respect to these performance requirements.

Induction machines have a wide speed range capability but relatively low power density. Synchronous reluctance have similar performance. The high torque ripple, vibration and loud noise in switched reluctance machines makes them not preferable for high performance electric drive applications such as automotive and aerospace [11], which require smooth torque.

Permanent magnet (PM) synchronous machines are the topology of choice owing to their high power density and their relatively high efficiency, due to the fact that the rotor magnetic fields are generated by permanent magnets, without conduction losses and external circuitry as in the case of field winding machines.

On the other hand, one issue with PM machines is that they can have a limited speed range, as the induced EMF on the stator windings increases as the rotor speed increases. This voltage can get as high as that of the DC link voltage of the inverter to the point that power can no longer be supplied to the machine.

The field-weakening control technique is used [21, 36] to deal with this issue and enables a much higher speed than would be possible otherwise. The field-weakening technique works by controlling the stator current components to generate a stator field that opposes the rotor field from the permanent magnets, reducing the magnitude of the induced EMF at a given speed.

A downside of this scheme is that, should a fault occur when implementing the field-weakening mode at high speed, the stator current is set to zero by the protection system but it will take some time for the rotor to come to stop and the full flux of the

PM rotor will be acting during this time. This can make the stator induced voltage to be much larger than the limits of the inverter or power electronics components connected.

Jahns and Refaie, investigated characteristics of these fault modes in [10]. As the field weakening implementation depends on the stator current, this is a **reliability** concern that goes along with extending the operating speed of permanent magnet machines. There are also possible issues with **demagnetization** of the magnets, through field weakening, aging or other environmental stresses while in operation, [3] .

Another major issue with PM machine designs is the cost of rare-earth materials used in high-performance magnets [24]. Moreover, the price is volatile, and there is also uncertainty on the long-term availability of these rare-earth materials. For example, recent prices for Neodymium-Iron-Boron, the most commonly used rare earth magnet in permanent magnet machines, have been listed as $\$60/lb$ [24] and $\$100/lb$ [8], which shows the volatility of the price.

The volatile cost of rare earth materials [19] , [8] has spurred interest in the development of high-performance electric machines and drives which do not require these materials. When compared to rare-earth permanent magnet machines, however, other conventional machine architectures for drives suffer from relatively low efficiency and power density.

A synchronous field-winding machine is another alternative for these applications. The operation of synchronous field winding machines is similar to rare-earth-based PM machines, the main difference being that electromagnets are used to produce the rotor flux instead of permanent magnets. As the main materials in field-winding machines are iron and copper, these machines have relatively low manufacturing cost.

Another major advantage of field-winding machines, compared to the PM machines, is the fact that the rotor field can be independently controlled. This capability

to control the rotor field makes the synchronous field winding machines suitable for high speed operation without the issue of reliability that exists in the PM machines, as the rotor flux is independently controllable and can be adjusted as needed. There won't be induced EMF on the stator, as the rotor field will disappear when the system shuts down due to faults. Field-winding machines are also used in high-performance applications like Auxiliary Power Units (APUs) in aerospace systems [11].

However, conventional synchronous field-winding machine designs possess a significant drawback which has historically prevented their use in many applications; **the need to provide power to the field coils on the rotor**. Efforts to improve their performance have been a research area for a long time now. Some of the major efforts, pertinent to this thesis, are discussed in the next section.

1.3 Brushless and Self-excited Schemes

The use of brushes and slip rings to transfer current to the rotor windings creates limits on the achievable speed, mechanical and electrical noise, mechanical wear, electromagnetic interference (EMI), and environmental compatibility issues (E.g. sparks from the brushes may cause fire in hazardous environments.). Also, considerable space is required for the brushes, slip rings, and external circuitry which produces the field-winding current, which makes it undesirable in applications where high power density is required.

Going "brushless" therefore has considerable advantages, and to this end a variety of brushless excitation mechanisms have been developed. Research in this area is still ongoing, improving different aspects of their implementation.

1.3.1 Related Works and Literature Review

The fundamental idea for most brushless operation techniques is based on the process of induction and rectification. In such machines, an auxiliary magnetic field source is used to induce alternating voltages in a winding mounted on the rotor; the induced voltage is then rectified and produces a DC component in the rotor field winding. Then the machine operates as a conventional synchronous field-winding machine.

Realization of brushless operation became possible with the introduction of compact high-power silicon rectifier diodes during the 1950s, as brushless excitation relies on diodes to rectify an induced AC voltage to achieve the DC field current. This and related studies enabled the first brushless generators to be built in the late 1950s, and the first large brushless motor went into service in the early 1960s, following the introduction of high-power thyristors for brushless schemes [6]. Figure 1.12 below shows the basic components and structure for brushless implementation.

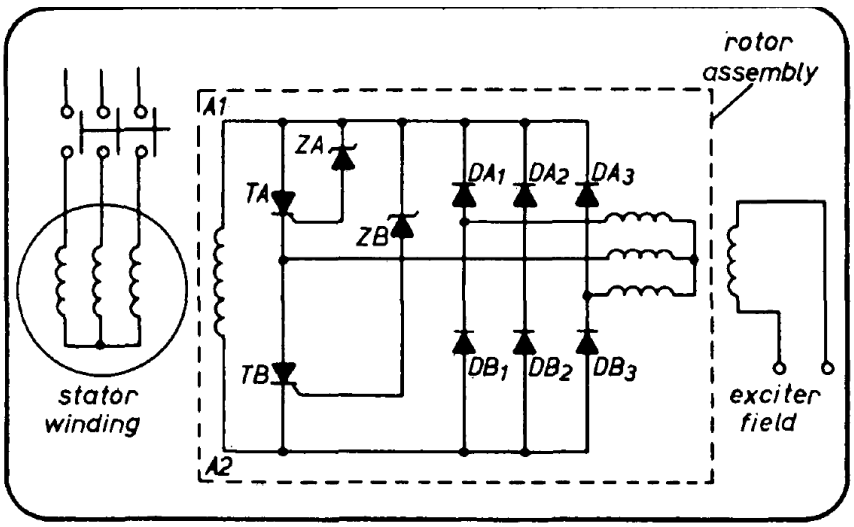

Figure 1.12: Three-phase-bridge brushless circuit [6]

This configuration, presented by Allen [6], consists of a conventional stator winding and additional exciter field winding in the stationary frame, which produces the main rotating field and the exciting DC field respectively. Mounted on the rotor shaft are three-phase armature windings, a three-phase rectifier, and the main synchronous machine field winding. As the rotor spins, the relative motion between the exciting DC field and the armature windings in the rotor induces EMF. The induced EMF on the armature windings is rectified, and the resulting DC voltage is applied to the field winding. In addition to exciter winding, this requires a separate exciter circuit where control of the rotor field is implemented, which adds size and weight to the generator.

Another configuration uses the main stator to supply power for the excitation. Vitay in [41] categorizes the mechanisms to produce a rotor field into three different approaches of inducing the voltage:

- by way of a power supply with multiple frequencies,
- through an unbalance in power supply, and
- through spatial harmonics in the motor windings.

Vitay also presented an implementation based on the idea of a stator supply having more than one frequency component, and consisting of a main field rotating at the synchronous speed and additional auxiliary magnetic fields rotating at different speeds, produced by an auxiliary coil. This induces an EMF which is rectified and supplies the field coils. The presence of the auxiliary circuit again adds to the weight of the machine. Furthermore, [41] does not discuss how the effect of torque ripple due to these multiple frequency components is mitigated. It also does not discuss specifics of how the auxiliary and field windings are implemented. A variation of [41] is also presented by Nonaka and Kesamaru in [28], where multiple spatial harmonic components are used, but this does not allow independent control of the field.

Vitay et. al. in [42] presented an improved version, the stator of which contains three-phase main and auxiliary windings, and the rotor contains an auxiliary winding, a diode bridge rectifier, a DC field winding, and optional short-circuit damper windings. Once again, these constituent components add to the size and weight of the machine, affecting its power density. To deal with possible coupling between the main and auxiliary fields, [42] also discussed the mechanism of the rotor having different pole numbers as compared to the main stator winding, which is a design constraint. Moreover, detail on control of the rotor field is not presented.

Inoue et.al. in [20] discussed a method using the fifth-space-harmonic component. It uses an additional reactor to generate the fifth-harmonic component, which adds to the size and weight of the machine. Moreover, this scheme lacks independent control of the rotor field.

A scheme was presented by Nonoka et al in [29] for a single phase generator application, where a voltage is induced in a field winding by a reverse revolving field due to single-phase armature reaction. A stationary DC coil on the stator was used to control the field, along with the field from the armature reaction. A variation of this brushless self-excited scheme is presented by Nonaka in [26], and has a stator with a

four-pole three-phase main winding and six-pole single-phase excitation winding. The excitation winding is supplied from an external DC source to induce a voltage on the rotor field coils, which is rectified to produce the field. The external DC source is also used to control the rotor field. In addition to the need for an external DC supply, the issue of very large voltage drops due to armature reaction is identified as a concern in this implementation. It also requires optimization of the pole arrangement between the main stator and exciter coils to deal with mechanical vibration issues.

Based on the idea of superimposing harmonics, Nonaka et al presented another scheme in [27]. Basically superimposing the fundamental and 5^{th} harmonics in the stator current, they also presented results using the DC and 5^{th} harmonic excitation and analysis for other harmonics as well. This scheme requires dual converters. They identified issues with modulation limits that arise while superimposing the harmonics.

Minor variations on this machine type using multiple stator windings have also been described by Nonaka [26] and Nonaka and Kesamaru [29]. This machine design allows for the independent control of main and auxiliary fields necessary to adequately control field currents in applications requiring field weakening. However, independent control of the main and auxiliary windings requires additional power electronic circuitry, either in the form of an independent power inverter, or in the form of a variable resistance that may be placed in-line with the stator auxiliary windings. This additional power electronic circuitry is undesirable from both a cost and reliability standpoint. The additional set of stator windings is also undesirable, as it takes up space that could be used by the main stator winding. This increases the resistance, and hence conduction losses, in the stator.

More recently, in 2014, a publication by Lipo et al, in [37], presented another implementation that can be considered as in the first or third category of [41], similar to what is presented in [28]. They discuss the use of a dual converter to inject a fundamental and third harmonic into the stator winding. However, the control

mechanism was not resolved. The idea of injecting a DC or high frequency current component is also analyzed, but experimental results were not presented. In addition, [37] also identified and discussed issues requiring future research, such as higher harmonic excitation in the field windings that can affect the establishment of a stable and controllable DC excitation current, start-up issues for motor operation, and need for means to obtaining an initial 3^{rd} harmonic current for generator operation. The specific implementation of the dual converter control to inject the harmonics is not discussed. This need for dual converter adds to the cost and size of the drive system.

1.4 Contribution of This Thesis

As of now, the PM machine is often considered as the best topology due to its high power density, relatively high efficiency, its CPWSR capability, and ease of control. However, their high cost due to the volatile price of rare-earth metals, and the fact that these rare-earth metals are scarce puts real concerns on the future price of these machines. There are also reliability concerns due to the possibility of demagnetization.

On the other hand, other machines perform poorly in the areas where the PM machines excel. A number of research ideas have been presented in order to improve the performance of synchronous field-winding machines, which suffer from relatively low power density, lower efficiency, and less reliability, mainly due to the slip-ring and brush assembly which is critical for their operation. So, coming up with better ways to improve or possibly eliminate these brush and slip-ring components from these machines has been a significant area of research.

This research work presents one such idea [36] that eliminates the need for brushes and slip rings, and that is also self-excited so no extra external circuitry is required. This method is based on the use of Field Oriented Control (FOC) techniques to induce a voltage on a rotor "transformer" winding that will then be rectified, hence producing the main rotor DC field required for its operation, (§ II) . This method, superimposing a high frequency carrier component on the stator current, is implemented on a conventional three-phase stator, without the need for additional modifications. Also, the converter used is a conventional three-phase converter with no modification as well. A prototype of the machine has been built and the method has been proven to work. It is the first time a machine of this type has been built.

The fact that it is done using conventional components, without an additional stator winding or external circuitry, contributes to improving the cost and power density of the machine.

In addition, an FEA-based simulation model of the proposed machine is developed. This model combines a rectifier circuit model with a magnetic model of the machine that accounts for magnetic saturation. It is used in the design of the prototype machine, and can be customized for specific design parameters as needed.

CHAPTER II

Proposed Machine Operation Principle and Drive Concept

2.1 Proposed Machine

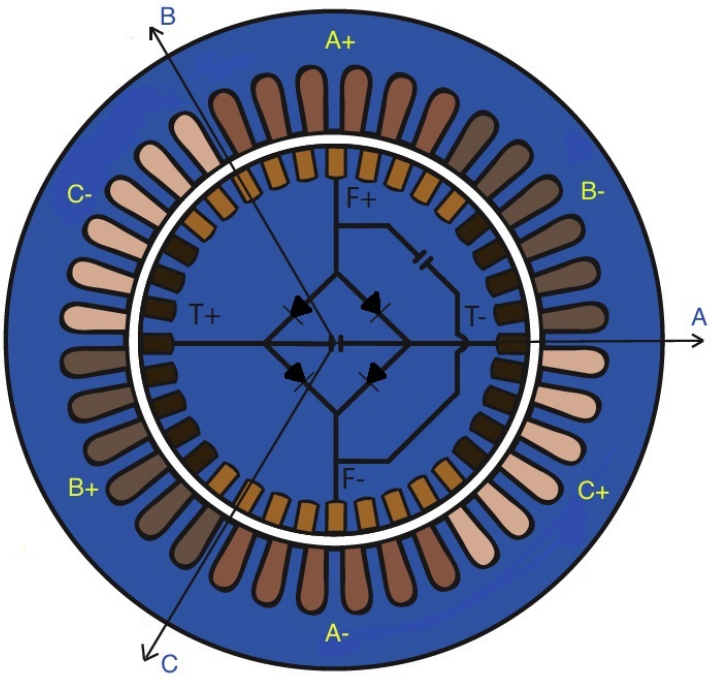

Figure 2.1: Cross-section of proposed brushless, self-excited synchronous field-winding machine, two-pole design, [33]

2.1.0.1 Operation Principle

This project explores an alternative brushless, self-excited synchronous field-winding machine design (BLSESFW). The design consists of a standard AC stator and a wound rotor with both field and transformer windings. A diode rectifier connects the two rotor windings. Figure 2.1 shows a cross section of a representative machine, depicting the idea of the proposed machine design. A 2-pole design is shown here, but the principle applies to machines having any other number of pole-pairs. It is also possible to have a magnetic saliency in the rotor design, though the one shown here is a non-salient type. The number of slots can be set as required by the design.

A two-phase machine model (§ 1.1.1.1) is considered, where the rotor windings are aligned with the direct (d) and quadrature (q) axes of the synchronous reference frame. The field-winding is oriented with the d axis, and the transformer-winding is oriented with the q axis.

Using the FOC control algorithm (§ 1.1.1.3) the d and q-axes currents are controlled appropriately. This ensures the decoupling of the excitation of the field and transformer windings. Hence, this avoids issues arising from coupling observed in other designs.

2.1.0.2 Drive Concept

Using standard field-oriented control techniques (FOC), (§ 1.1.1.3), an oscillating current component is superimposed on the q-axis stator current (i_{sq}), which is aligned with the transformer winding. This oscillating current produces an AC magnetic field on the transformer winding of the rotor, which in turn induces an electro-motive-force (EMF) in the transformer winding. This induced EMF is rectified into a DC voltage by a rectifier circuit mounted on the rotor, and hence supplies the field winding with DC voltage.

The quadrature component of the stator current i_{sq} will therefore have two compo-

nents, a fundamental component for torque production and a superimposed oscillating component (carrier component), used to induce voltage on the transformer winding of the rotor. The d-axis stator current, i_{sd}, will be used to mitigate possible torque ripple as needed, or used for field-weakening. The magnitude and the frequency of the carrier component can be independently controlled, and therefore the magnitude of the field current is controlled through the carrier component.

Issues with the PM machines related to faults during high speed operation and lack of control over the rotor flux are resolved with this design, which is particularly significant at high speed operations of the machine. In the PM machines case, magnetic flux in the rotor is from permanent magnets with fixed flux density. The voltage induced on stator winding from the rotor field is proportional to the speed of the rotation. Under normal operation this induced voltage is limited due to the BEMF from the stator field, even at high speed. Should a fault occur while running at high speed, however, the stator winding field will go to zero as the stator currents are set to zero by the protection system. But the rotor will still have its magnetic field from the permanent magnet and at such high speed the induced voltage from rotor magnets will reach very large magnitude that can damage the power electronics circuitry as well as the insulation of the stator winding. In this presented design, there will not be such induced voltage as the totor field is set to zero with the stator current.

In addition to vehicular applications, the proposed motor design could replace induction machines in many variable-speed drive applications. It is shown that the proposed machine can be more efficient than induction machines and provide more power for a given RMS current.

CHAPTER III

Finite Element Analysis and Modeling (FEA)

3.1 Significance of FEA

Lumped-parameter models can demonstrate the basic behavior of an electric machine, but are not ideal for design purposes, as the model parameters (e.g., inductance and resistance) are inherently approximate by nature. For example, typical lumped-parameter models assume linear magnetic behavior, and hence do not capture the important effect of magnetic saturation. Furthermore, lumped-parameter models typically assume a smooth airgap, and hence do not model the effects of the slotting of the stator and rotor iron.

As a result, finite element analysis (FEA) is often used in the design of electric machines[44][13]. FEA models are directly constructed from machine geometric parameters and material properties, which makes them ideal for design purposes[34][25]. FEA models also allow the accurate capture of phenomena such as saturation and slotting effects.

The proposed machine differs from conventional electric machine designs due to the presence of electronic circuitry internal to the machine. The full-bridge diode rectifier is mounted on the rotor of the machine and used to rectify the induced voltage from the transformer winding and supply the field winding with DC voltage. The model should therefore also incorporate this electronic circuitry. As a result, a

finite-element model which incorporates the diode rectifier model has been developed.

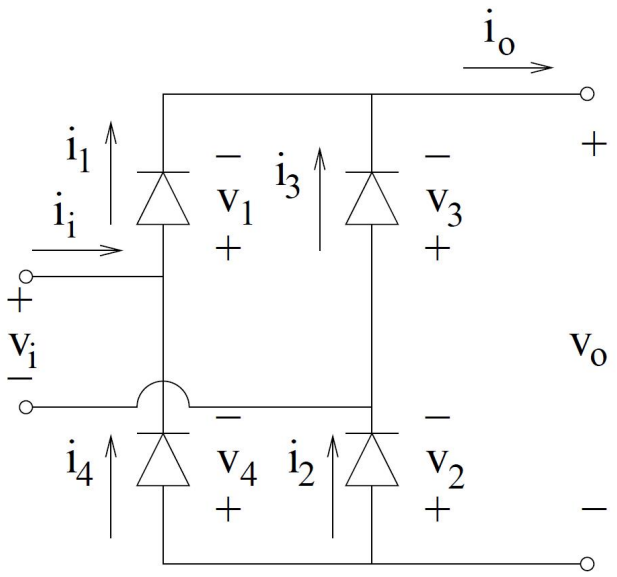

Figure 3.1: Full-bridge diode rectifier circuit

3.2 Models and System Equations

3.2.1 Rectifier Model

A full-bridge diode rectifier is represented by the circuit shown in Figure 3.1. It is a two-input two-output model [33]. For our purposes we will consider the rectifier voltages as inputs and the currents as outputs.

Exploiting symmetries in the operation of the rectifier, we can define variables v_+,v_-, i_+, and i_- as follows:

$$v_+ = v_1 = v_2 \tag{3.1a}$$

$$v_- = v_3 = v_4 \tag{3.1b}$$

$$i_+ = i_1 = i_2 \tag{3.1c}$$

$$i_- = i_3 = i_4 \tag{3.1d}$$

It can be shown that

$$v_+ = 1/2(v_i - v_o) \tag{3.2a}$$

$$v_- = -1/2(v_i + v_o) \tag{3.2b}$$

$$i_+ = f_d(v_+) \tag{3.2c}$$

$$i_- = f_d(v_-) \tag{3.2d}$$

$$i_i = i_+ - i_- \tag{3.2e}$$

$$i_o = i_+ + i_- \tag{3.2f}$$

These expressions can be lumped into a single, nonlinear vector function

$$\vec{i}^r_{rect} = \vec{f}_{rect}(\vec{v}^r_r) \tag{3.3a}$$

where

$$\vec{i}^r_{rect} = \begin{bmatrix} -i_i \\ i_o \end{bmatrix},$$

$$\vec{v}^r_r = \begin{bmatrix} v_i \\ v_o \end{bmatrix}$$

The sign of the input current is changed in the vector in order to have a consistent polarity of the currents (i.e., leaving the positive terminals of the voltages).

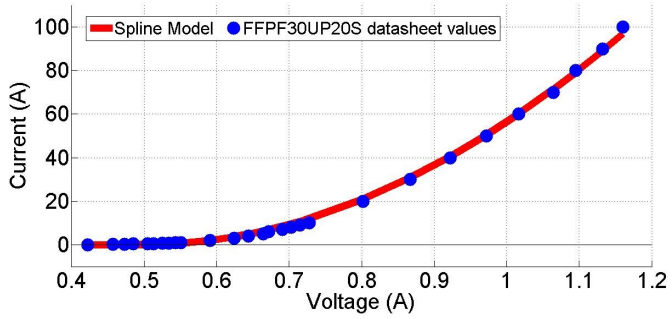

Figure 3.2: Cubic spline model of $V - I$ diode characteristics

3.2.2 Diode Model

The current-voltage relationship of the diodes, $i_d = f_d(v_d)$, is given in Shockley equation by

$$i_d = I_o(e^{v_d/V_t} - 1) \tag{3.4}$$

where I_o is the diode reverse saturation current and $V_t = kT/q$ is the thermal voltage.

However, in our model we generate $f_d(.)$ through the use of cubic spline interpolation of the datasheet $v - i$, diode characteristics which allows us to match empirical data while at the same time guaranteeing continuity and differentiability of the function, as shown in Figure 3.2. Using this diode model, the rectifier model is implemented.

3.2.3 FEA Machine Model

A custom FEA magnetostatic model, written in MATLAB ® is used to solve the field equations. This model captures the nonlinear property of magnetic saturation by modeling ferromagnetic materials with a field-dependent equivalent current density, [30].

3.2.3.1 Maxwell's Equations

The basis for this type of problem are Maxwell's electromagnetic equations. The relevant Maxwell's equations [31], applicable for this machine design are

$$\nabla \cdot \mathbf{B} = 0 \qquad \text{Gauss's law for magnetism} \tag{3.5a}$$

$$\nabla \times \mathbf{E} = -\frac{\partial \mathbf{B}}{\partial t} \qquad \text{Faraday's law of induction} \tag{3.5b}$$

$$\nabla \times \mathbf{H} = \mathbf{J} + \frac{\partial \mathbf{D}}{\partial t} \qquad \text{Ampère's law} \tag{3.5c}$$

In these equations, $\mathbf{J}$ is the electric current density, $\mathbf{E}$ is the electric field intensity, $\mathbf{H}$ is the magnetic field intensity, $\mathbf{D}$ is the electric flux density which is neglected in this formulation as the frequency if relatively low for the displacement current to have an impact, and $\mathbf{B}$ is the magnetic flux density.

3.2.3.2 Constitutive Relations

It is assumed that the electric current density is isotropically related to the electric field intensity

$$\mathbf{J} = \sigma \mathbf{E}, \tag{3.6}$$

and the following constitutive relationship between $\mathbf{B}$ and $\mathbf{H}$ is considered, [30]

$$\mathbf{H} = \frac{\mathbf{1}}{\mu_\mathbf{0}}\mathbf{B} - \mathbf{M}(\mathbf{B}), \tag{3.7}$$

where $\mathbf{M}$) is magnetization as a function of the magnetic flux density, σ is the electrical conductivity of the material, and $\mu_0 = 4\pi \cdot 10^{-7}\frac{H}{m}$ is the permeability of free space.

3.2.3.3 Derivation of The Field Equation

From (3.5c), considering the magnetoquasistatic assumptions, neglecting the displacement current component of Ampere's law, and substituting equations (3.6) and (3.7) gives

$$\frac{\mathbf{1}}{\mu_\mathbf{0}}\nabla \times \mathbf{B} - \nabla \times \mathbf{M} = \sigma\mathbf{E} = \mathbf{J} \tag{3.8}$$

From (3.5a) we have $\nabla \cdot \mathbf{B} = 0$ implies that $\mathbf{B}$ can be written as the curl of a vector, and hence the magnetic vector potential, A, is defined as the vector satisfying the relation

$$\mathbf{B} = \nabla \times \mathbf{A} \tag{3.9}$$

Substituting this into (3.8) gives:

$$\frac{\mathbf{1}}{\mu_\mathbf{0}}\nabla \times \nabla \times \mathbf{A} - \nabla \times \mathbf{M} = \mathbf{J} \tag{3.10}$$

The machine we are considering in this design is of cylinderical geometry. Also, the electric fields and currents are mostly aligned along the z-axis of the machine due to the winding construction.It is therefore a reasonable assumption to consider the magnetic flux to be in the x-y plane, and hence the vector potential to be pointing in the z-direction. For this reason a two-dimensional model of the machine is considered.

In this two-dimenstional analysis, A_z is the only component of the magnetic vector potential. With $\nabla^2 A_z = (\frac{\partial A_z}{\partial y}\hat{x} - \frac{\partial A_z}{\partial x}\hat{y})$ and $\nabla' = (-\frac{\partial}{\partial y}\hat{x} + \frac{\partial}{\partial x}\hat{y})$, and considering

the vector identity $[\nabla \times \nabla \times (\mathbf{A}) = \nabla(\nabla \cdot (\mathbf{A})) - \nabla^{\mathbf{2}}(\mathbf{A})]$, and the coulomb gauge, $(\nabla \cdot \mathbf{A} = \mathbf{0})$, (3.10) becomes

$$\frac{1}{\mu_0}\nabla^2 A_z - \nabla^{'} \times \mathbf{M}(A_z) = J_z \tag{3.11}$$

$$\frac{1}{\mu_0}\nabla^2 A_z - J_m = J_z \tag{3.12}$$

which defines the field equation, where J_m is equivalent magnetization current density.

3.2.3.4 Boundary Conditions, [30]

The boundary conditions define the behavior of the fields at the boundary of the material under consideration. These conditions used in this modeling of the machine are described next.

Periodic Boundary Condition

In two-dimensional analysis, in polar coordinates, the magnetic vector potential exhibits the symmetry

$$A_z(\phi) = A_z(\phi + 2\pi f_p k) \tag{3.13}$$

with $f_p = p/N_p$, p even, and N_p is the number of machine poles, and k is arbitrary integer.

There is also another symmetry known as antiperiodicity, with p odd, expressed as

$$A_z(\phi) = -A_z(\phi + 2\pi f_p k) \tag{3.14}$$

Using the antiperiodic boundary condition, the model can then be restricted to a fraction f_p of the machine.

In the present case, a machine design with 4-poles, only one pole of the machine need be modeled and the remaining portions are determined making use of the anti-periodic boundary condition.

Dirchlet Boundary Condition

With in the dimensions of the machine under consideration, the boundary for the solution of the field equations is chosen sufficiently large so that the field can safely be assumed that there is no magnetic flux in near the boundaries. Hence,

$\mathbf{B} \cdot \mathbf{n} = \mathbf{0}$ on Γ_0, where $\mathbf{n}$ is the unit normal vector to the boundary Γ_0 which also implies that $\mathbf{A} = \mathbf{0}$ on Γ_0, as $\mathbf{B} = \nabla \times \mathbf{A}$ and the assumption of antiperiodicity above.

Neumann Boundary Condition

The Neumann boundary condition prescribes thetangential magnetic field component on the material boundary. Hence,

$\mathbf{H} \times \mathbf{n} = H_t$ on Γ_t, which is used along with the Boundary Transfer Relations below,

Boundary Transfer Relations [1]

The boundary transfer relations are defined for a cylindrical domain with inner boundary Γ_β and radius β, and outer boundary Γ_α with radius α, which represents the cylinderical annuli of the airgap between the rotor and the stator, and under the assumption that the magnetic vector potential on each boundary can be decomposed into a sum of spatial harmonics in the θ direction,

$$A(\alpha, \theta) = \sum_k A_k^{\alpha} \tilde{e}^{jk\theta} \tag{3.15}$$

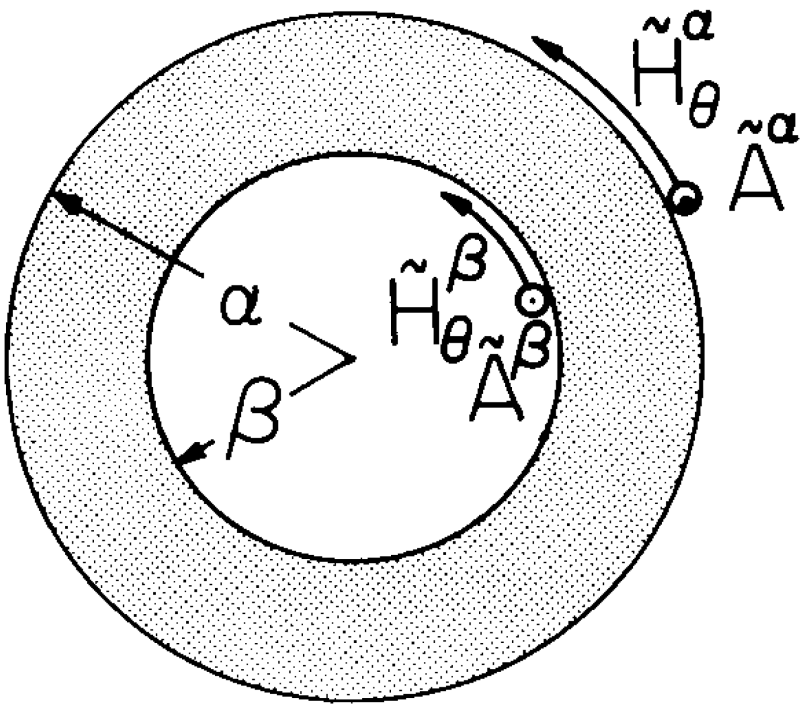

Figure 3.3: Vector potential transfer relations for two-dimensional polar coordinate

and

$$A(\beta,\theta) = \sum_k A_k^{\beta} \tilde{e}^{jk\theta} \tag{3.16}$$

and solution of the form

$$\tilde{A}_k(r,\theta) = \tilde{A}_k(r) e^{jk\theta} \tag{3.17}$$

The field intensity harmonics can then be written as:

$$\mathcal{H}_t^{\alpha} = \tilde{\mathcal{F}}_k(\beta,\alpha)\tilde{A}_k^{\alpha} + \mathcal{G}_k(\tilde{\alpha},\beta)\tilde{A}_k^{\beta} \tag{3.18}$$

$$\mathcal{H}_t^{\beta} = \tilde{\mathcal{G}}_k(\beta,\alpha)\tilde{A}_k^{\alpha} + \mathcal{F}_k(\tilde{\alpha},\beta)\tilde{A}_k^{\beta} \tag{3.19}$$

where

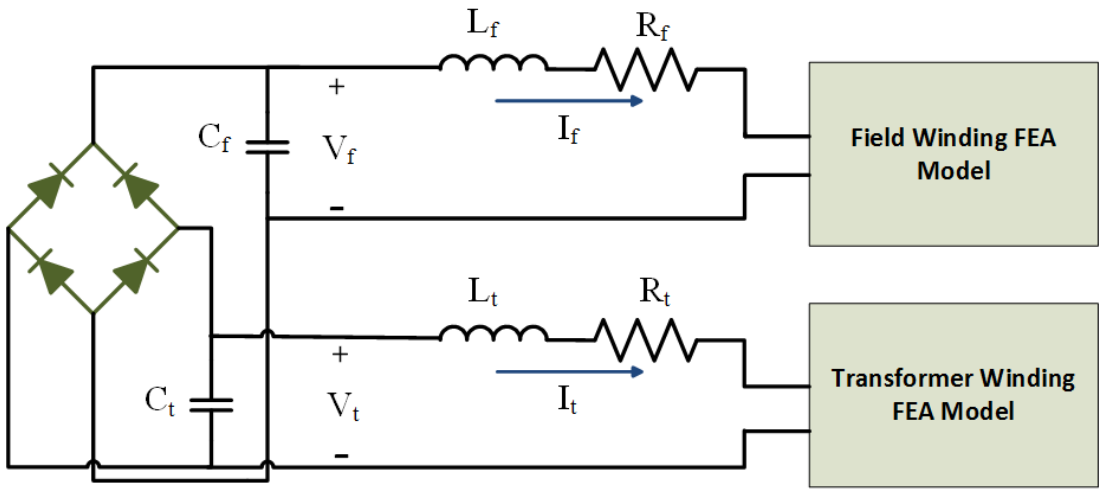

Figure 3.4: Schematic representation of the machine and rectifier model interface

$$\mathcal{F}_k(x,y) = \frac{1}{\mu_0}\frac{k}{y}\frac{(\frac{x}{y})^k + (\frac{y}{x})^k}{(\frac{x}{y})^k - (\frac{y}{x})^k}$$

$$\mathcal{G}_k(x,y) = \frac{2k}{\mu_0 x}\frac{1}{(\frac{x}{y})^k - (\frac{y}{x})^k}$$

3.2.4 Overall System Equations

The FEA model is then interfaced with a circuit model consisting of the diode rectifier and the resistances and end-turn inductances of the field and transformer windings, as shown in Figure 3.4.

Defining rotor current and voltage vectors as follows:

$$\vec{i}^r_{rect} = \begin{bmatrix} i_t \\ i_f \end{bmatrix}, \text{ and } \vec{v}^r_r = \begin{bmatrix} v_t \\ v_t \end{bmatrix} \tag{3.20}$$

where subscripts t and f correspond to the transformer and field windings, respectively. The overall system equations can then be written as:

$$\text{FEA Equation:} \quad \underline{K}_\theta \vec{a} = \vec{i}_m(\vec{a}) + \underline{B}_s \vec{i}_s + \underline{B}_r \vec{i}_r^r \tag{3.21a}$$

which is derived from the field equation (3.12) by formulating the FEA equation using the method of weighted residuals, (Galerkin's approach), [30]. The formulation is based on triangular elements, from which thematrices are assembled.

$$\text{Voltage Equation:} \quad \vec{v}_r = \underline{R}_r \vec{i}_r + \underline{L}_r \frac{d\vec{i}_r}{dt} + \underline{F}_r \frac{d\vec{a}}{dt} \tag{3.21b}$$

which is derived applying Kirchoff's voltage law and Faraday's law in Figure 3.4, along with the relation $\vec{\lambda}_r = \underline{F}_r \vec{a}$, where $\vec{\lambda}_r$ is the flux-linkage of the rotor windings in the FEA model.

$$\text{Current Equation:} \quad \underline{C}_r \frac{d\vec{v}_r}{dt} = \vec{i}_{rect} - \vec{i}_r = \vec{f}_{rect}(\vec{v}_r) - \vec{i}_r \tag{3.21c}$$

which is derived applying Kirchoff's current law in Figure 3.4.

In these expressions $\vec{a}$ is the nodal magnetic vector potential, $\underline{K}_\theta$ is the FEA reluctivity matrix (dependent upon rotor position θ), $i_m(\vec{a})$ is the nonlinear nodal magnetization current, $\underline{B}_s$ and $\underline{B}_r$ map the stator and rotor currents into FEA nodal currents, $\underline{F}_r$ maps the nodal magnetic vector potentials into rotor winding flux-linkages, and $\underline{R}_r$, $\underline{L}_r$ and $\underline{C}_r$ are diagonal matrices whose diagonal components consist of the transformer and field winding resistances, capacitances, and leakage inductances, respectively.

By applying Backward Euler integration, we can combine these three equations into a function, $\vec{f}(\vec{x})$, where

$$\vec{x}[k+1] = \begin{bmatrix} \vec{a}[k+1] \\ \vec{i}_r[k+1] \\ \vec{v}_r[k+1] \end{bmatrix} \tag{3.22}$$

We can therefore determine the states at each time step by solving the nonlinear equations

$$\vec{f}(\vec{x}[k+1]) = \begin{bmatrix} \underline{K}_\theta \vec{a}[k+1] - i_m(\vec{a}[k+1]) - \underline{B}_s \vec{i}_s[k+1] - \underline{B}_r \vec{i}_r[k+1] \\ \underline{F}_r \frac{(\vec{a}[k+1]-\vec{a}[k])}{h} + \underline{L}_r \frac{(\vec{i}_r[k+1]-\vec{i}_r[k])}{h} + \underline{R}_r \vec{i}_r[k+1] - \vec{v}_r[k+1] \\ \underline{C}_r \frac{(\vec{v}_r[k+1]-\vec{v}_r[k])}{h} + \vec{i}_r[k+1] - \vec{f}_{rect}(\vec{v}_r[k+1]) \end{bmatrix} = 0, \tag{3.23}$$

where h is the time step. This is achieved by applying the Newton-Raphson method, whose i^{th} iteration is given as follows:

$$\vec{x}_i = \vec{x}_{i+1} - \left(\frac{\partial \vec{f}}{\partial \vec{x}} \right)^{-1} \vec{f}(\vec{x}_{i-1}) \tag{3.24}$$

where the Jacobian matrix of the system is given by

$$\vec{J} = \frac{\partial \vec{f}}{\partial \vec{x}} = \begin{bmatrix} (\underline{K}_\theta - \frac{\partial \vec{i_m}(\vec{a})}{\partial \vec{a}} & \underline{B}_r & \underline{0} \\ \frac{1}{h}\underline{F}_r & (\frac{1}{h}\underline{L}_r + \underline{R}_r) & \underline{I} \\ \underline{0} & \underline{I} & (\frac{1}{h}\underline{C}_r - \frac{\partial \vec{f}_{rect}}{\partial \vec{v}_r}) \end{bmatrix} \tag{3.25}$$

and the Jacobian of the rectifier circuit is given by:

$$\frac{\partial \vec{f}_{rect}}{\partial \vec{v}_r} = \frac{1}{2} \begin{bmatrix} -\left(\frac{\partial f_d}{\partial v_d} + \frac{\partial f_d}{\partial v_d} \right) & \left(\frac{\partial f_d}{\partial v_d} - \frac{\partial f_d}{\partial v_d} \right) \\ \left(\frac{\partial f_d}{\partial v_d} - \frac{\partial f_d}{\partial v_d} \right) & -\left(\frac{\partial f_d}{\partial v_d} + \frac{\partial f_d}{\partial v_d} \right) \end{bmatrix} \tag{3.26}$$

CHAPTER IV

Prototype Machine Design

4.1 Magnetic Design and Simulation

The FEA simulation model is used to perform the magnetic design for the prototype machine. A four-pole machine is considered with a three-phase stator having 36 slots and a rotor having 28 slots, with transformer-to-field winding slot ratio of $\frac{2}{5}$. Dimensions of the machine are constrained by the reference induction machine that we identified for performance comparison, an Azure Dynamics AC24LS 4-pole Induction machine. We are using the same stator from the reference induction machine for the prototype machine, and hence the only difference between two machines is their rotor design. Measured dimensions from the reference induction machine are used for the design and simulation of the prototype machine.

Due to the symmetry of the machine, only one pole of the geometry is considered for simulation, which will save computation resources and time. Figures 4.1 and Figure 4.2, respectively, show the mesh and magnetic flux density plots from simulation.

From the simulation, the rotor geometric parameters are determined. The rotor design is also constructed from laminations to minimize eddy current losses in the rotor. The thickness of the lamination was determined to be 0.356 mm, an achievable minimum thickness taking manufacturing cost into account. One of these laminations

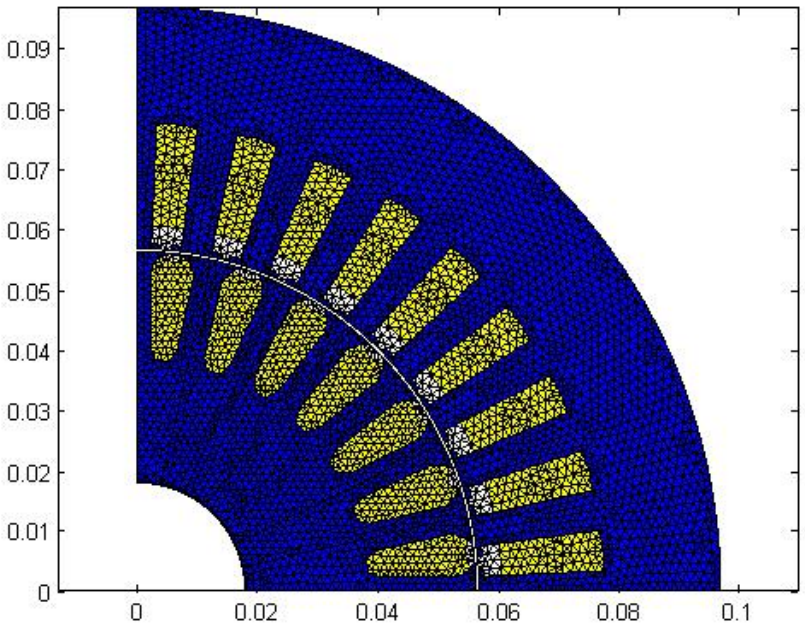

Figure 4.1: One-pole machine geometry with applied triangular FEA mesh

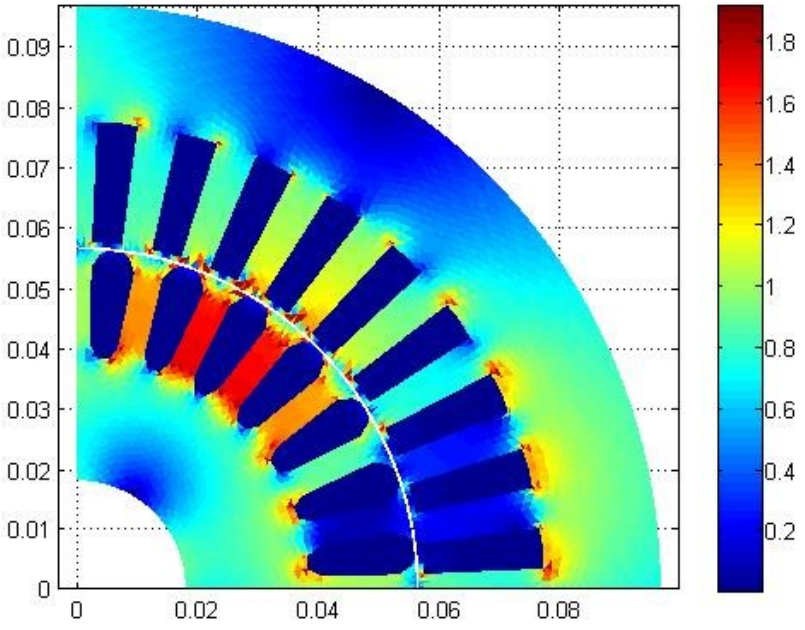

Figure 4.2: Flux density magnitude, $|B|$ in Tesla, of FEA Model simulation for one-pole of the machine

is shown in Figure 4.3. The laminations are stacked together and the rotor stack has a total length of 128 mm, as shown in Figure 4.4.

The rotor has a total of 28 slots, 8 for the transformer winding and 20 slots for the field winding. The rotor coils are made of inverter grade Essex magnet wires, with size 19 AWG for the field winding and 17 AWG for the transformer winding. The transformer winding design has 15 turns per slot, and the field winding has 45 turns per slot. The individual transformer coils are connected together in series, as are the field coils. By placing the windings in series we increase the voltage levels of the windings, and hence minimize the effects of the diode drops in the rectifier.

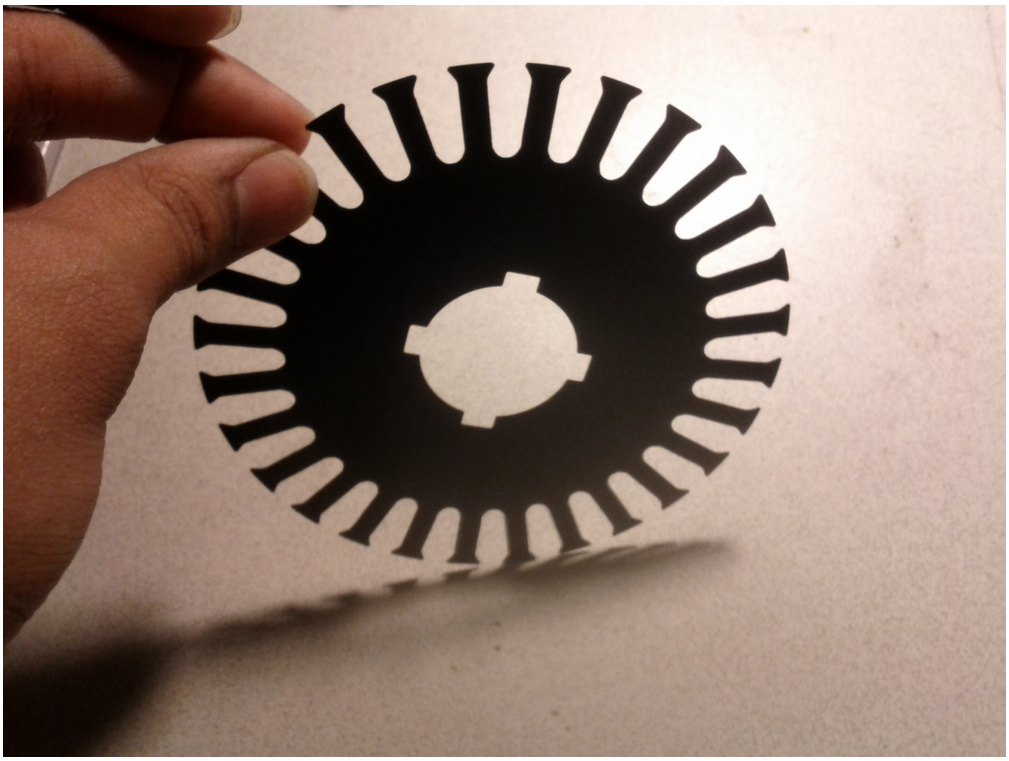

Figure 4.3: Rotor lamination

Figure 4.4 also shows a picture of the prototype rotor built, which has four terminals to be connected to the input and output of the full-bridge diode rectifier circuit.

The diode rectifier circuit on the rotor was built using discrete Schottky diodes. (Part No. FFPF30UP20STU). Ceramic capacitors were used with a 2.2μF capacitor

Figure 4.4: Prototype rotor

at the rectifier input (transformerwinding terminals) and a 6.8μF capacitor at the rectifier output (field-winding terminals). Aluminum end-caps are attached at both ends of the rotor. These provide a heat sink for the diodes and capacitors, plus cooling fins to help dissipate heat from the rotor. The measured inductance values are 8mH

for the transformer, and 280mH for the field windings of the rotor.

Figure 4.5 shows a picture of the rectifier circuit mounted on the cooling fins of the rotor. Two end-caps, with fins, were designed for two purposes: to help remove heat from the windings, and to create space for mounting the rectifier circuit.

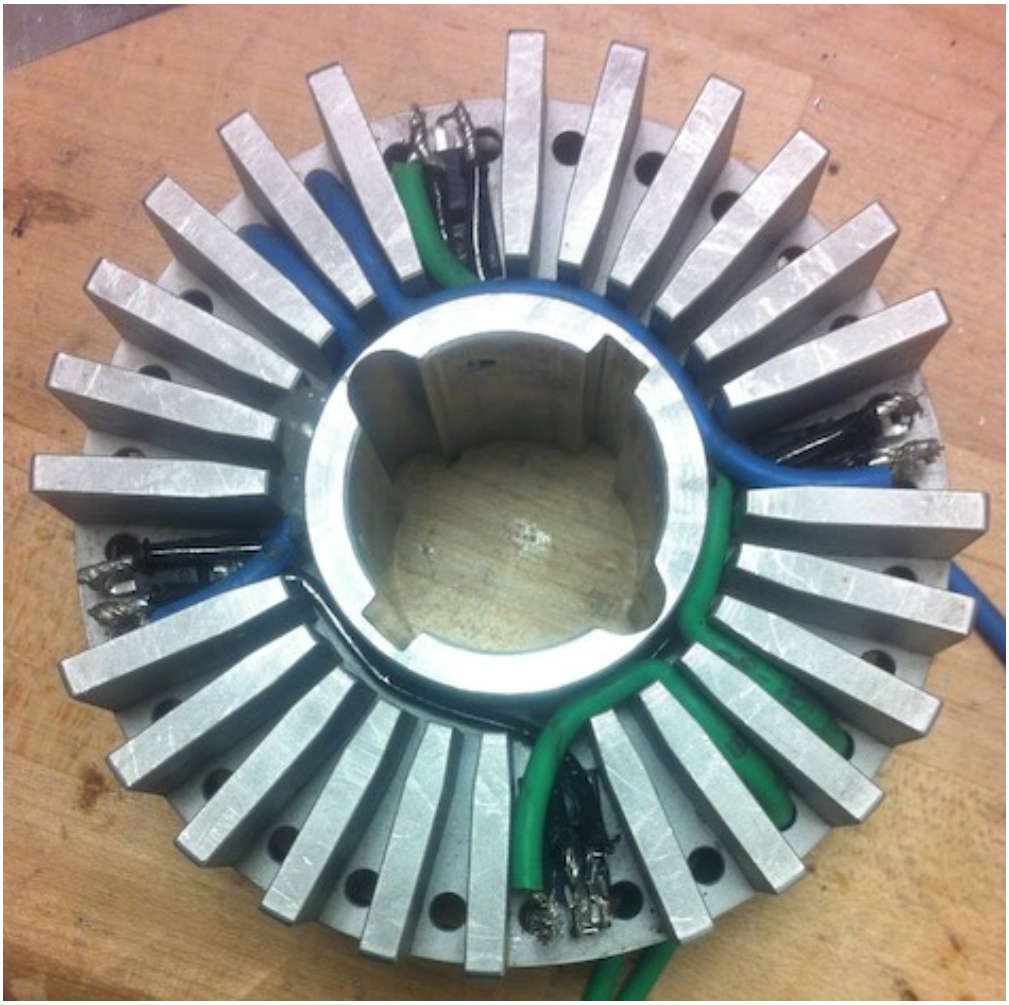

Figure 4.5: Prototype rectifier circuit mounted on cooling fins

A rotor shaft was also custom-made for the prototype with extension to mount the encoder. The complete rotor assembly is shown in Figure 4.7.

Figure 4.6: Assembled rotor stack and winding

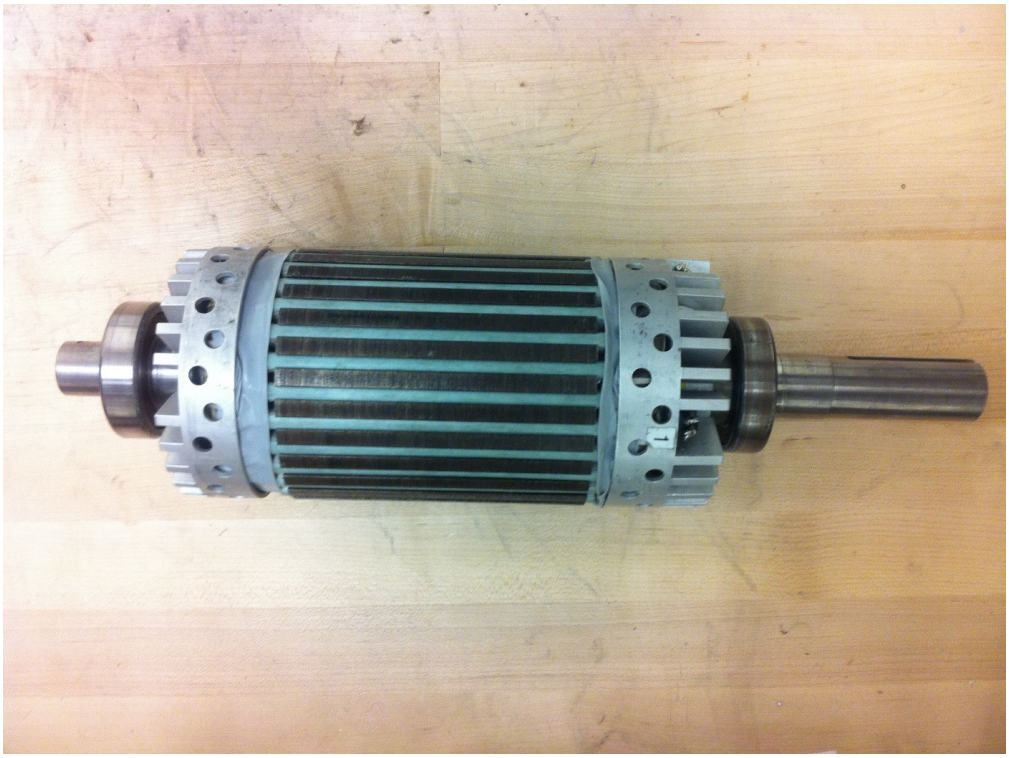

Figure 4.7: Assembled rotor of prototype machine

4.2 Thermal Simulation and Design

(Work performed by Prerit Terway, Masters Student)

A steady state temperature distribution of the motor was obtained by performing thermal simulation on the 3D model of the motor by using SolidWorks Flow Simulation. Custom fins were used to cover the end turns as well as to enhance cooling from rotation of the rotor. A steady-state computational fluid dynamics simulation was performed on the machine, with the rotor spinning at 3000 rpm. Table 4.1 shows the various parameters used for thermal simulation. In order to simplify the analysis, the same power loss density was assumed for the field and transformer windings in the rotor slots. The cooling effect produced due to the rotation of the fins was captured by incorporating the effect of rotation during simulation. The external condition was assumed to be air at a temperature of 25^oC. The maximum temperature of the motor as can be seen from Figure 4.8 is less than 150^oC (which is the maximum permissible temperature for Class H insulation).

Table 4.1: Thermal simulation parameters

Parameter	Value
Power loss density for stator slots	560000 W/m3
Power loss density for rotor slots	846980 W/m3
Power loss density due to core losses	55700 W/m3
Rotor Speed	3000 rpm
Ampere turns assumed for rotor slots	390 A-turns

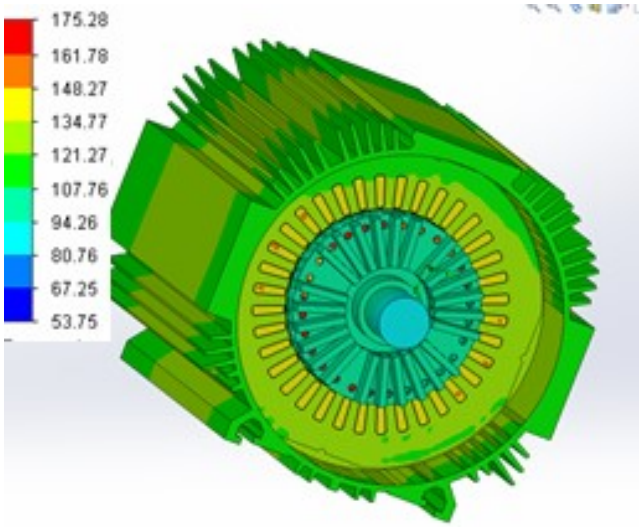

Figure 4.8: Temperature distribution of the machine under maximum power conditions, calculated using computational fluid dynamics

CHAPTER V

Experimental Setup

5.1 Experimental Setup

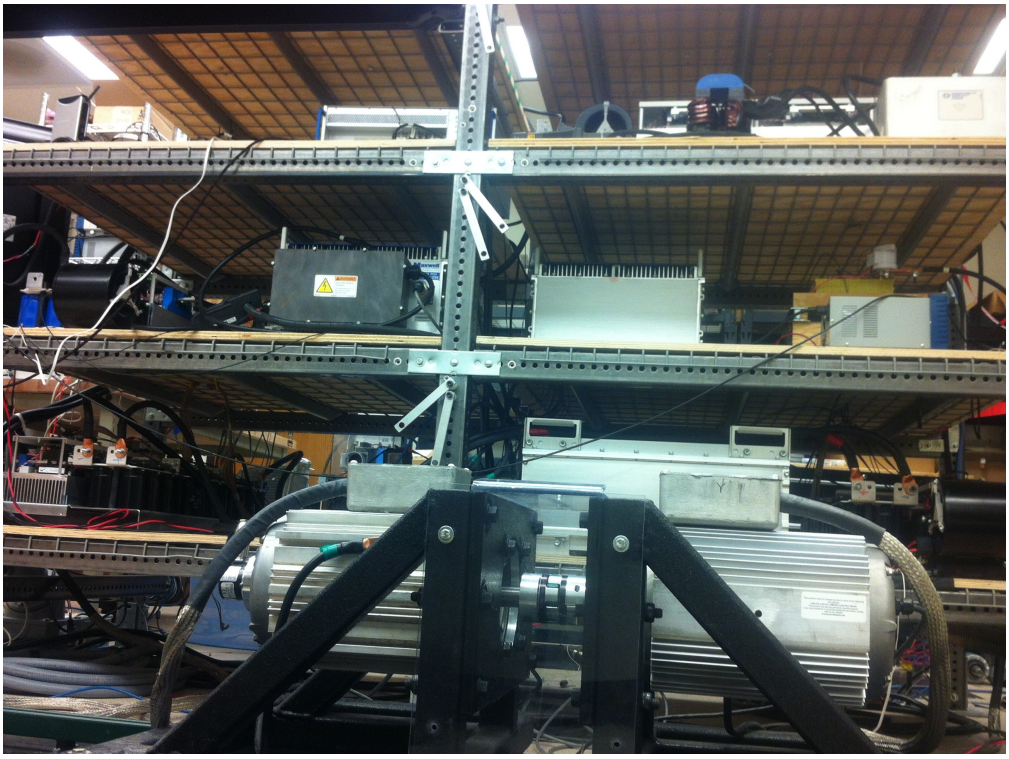

Figure 5.1: Machine test fixture setup showing the prototype machine (left: Machine 1) coupled to the driving/loading induction machine (right: machine 2), both having the same stator and differing in their rotor construction.

For the experiments, an Azure Dynamics AC24 76WGW079 induction machine is used as the load for the prototype machine. In addition, a T2-500-C6A torque

transducer from Interface Inc. is used to measure torque. Two sets of IAP600T120 3-phase IGBT inverters made by APS (rated at 600A/1200V) are used to power the prototype machine and the induction machine. In the following test, the inverters operate on a 280V DC bus. A real-time simulation and testing tool is used to design and implement the control algorithm. It is the Speedgoat GmbH dual-core Intel i3 CPU processor with an IO106-32 A/D converter and IO312 FPGA boards for PWM generation and quadrature encoder interface, using auto-generated code from MATLAB/Simulink. Fig. 7 shows the test setup, and the prototype machine coupled with the induction machine, which regulates the speed.

The prototype machine has the same stator as the reference induction machine. A 10 kHz switching frequency and 280 V DC bus voltage are applied to the inverters. The motor is spun applying conventional FOC to regulate the quadrature axis current, using Space-Vector Modulation (SVM) to generate the duty-cycle, applied to the inverter. The duty cycles are updated every switching period, the ADC sampling is synchronized with center-based PWM signals to avoid possible noise induced by switching transients. An H58 series shaft encoder, H582540111353, from Dynapar is used for rotor angle measurement used for the SVM implementation. In addition a multi-channel precision power analyzer, LMG670 with bandwidth DC-10 MHz, from ZES Zimmer Inc. is used for inverter power measurement.

CHAPTER VI

Experimental and Simulation Results

Simulation and experimental, results of **open-circuit**, **locked-rotor** and **spin** tests are presented in this chapter. In addition, a performance comparison between the prototype machine and an induction machine is also presented. For this comparison, the spin test is performed on the same exact stator, and the difference between the two machines is made by swaping the corresponding rotor for each case.

6.1 Open-Circuit Test

6.1.1 Simulation

The open-circuit test in simulation is performed by disabling the rectifier circuit model of the FEA machine model and computing the terminal voltage at the transformer and field windings. Voltage will be induced in the rotor windings from the stator magnetic flux. The stator flux is directed along the stator direct-axis and, depending on the rotor position, this flux links with the rotor windings. Hence, the magnitude of the induced voltages depend on the position of the rotor with respect to the direct-axis of the stator winding. The maximum voltage at each rotor winding is expected when they are aligned with the direct-axis where the fllux linking the winding is maximized. So the simulation is done by first aligning the rotor accordingly. This test verifies the performance of the transformer action, which is the basis for the operation of this machine.

6.1.2 Experiment

The open-circuit test in experiment is performed by physically disconnecting the rectifier circuit and measuring the terminal voltage at the transformer and field windings. Once again, these voltages depend on the position of the rotor with respect to the direct-axis of the stator winding. Similarly, voltage will be induced in the rotor windings from the stator magnetic flux. Hence, the magnitude of the induced voltages depends on the position of the rotor with respect to the direct-axis of the stator winding. The maximum voltage at each rotor winding is expected when they are aligned with the stator flux to maximize the flux linking each winding. This angle alignment is achieved using measured rotor position information and adding appropriate offset as needed.

6.1.3 Results

Figure 6.1 and Figure 6.2 below respectively show the simulation and experiment result for the field-winding and transformer-winding voltages. This test is performed by applying stator quadrature-axis current with a carrier component of 5A at 100 Hz frequency, and setting the fundamental component of the stator quadrature axis current to zero. In this case the rotor angle is adjusted so that the stator direct-axis is aligned with the field winding.

Figure 6.3 and Figure 6.4 respectively show simulation and experimental result of the open-circuit test voltages for field and transformer windings of the rotor. In this case, a carrier current component of 5A,100 Hz carrier is applied, with the rotor position set so that the carrier field aligns with the corresponding winding of the rotor. In this case the rotor angle is adjusted so that the stator direct-axis is aligned with the transformer winding.

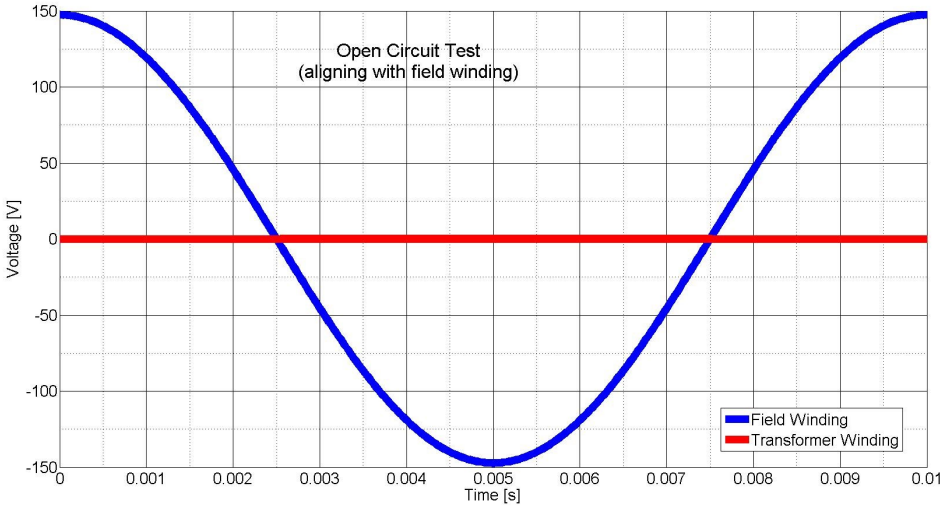

Figure 6.1: Open-circuit test rotor voltages: stator flux aligned with field-winding, simulation results

We notice from the figures that the voltage induced at the unexcited winding is close to zero, as the two windings are in quadrature, and therefore verify that they are

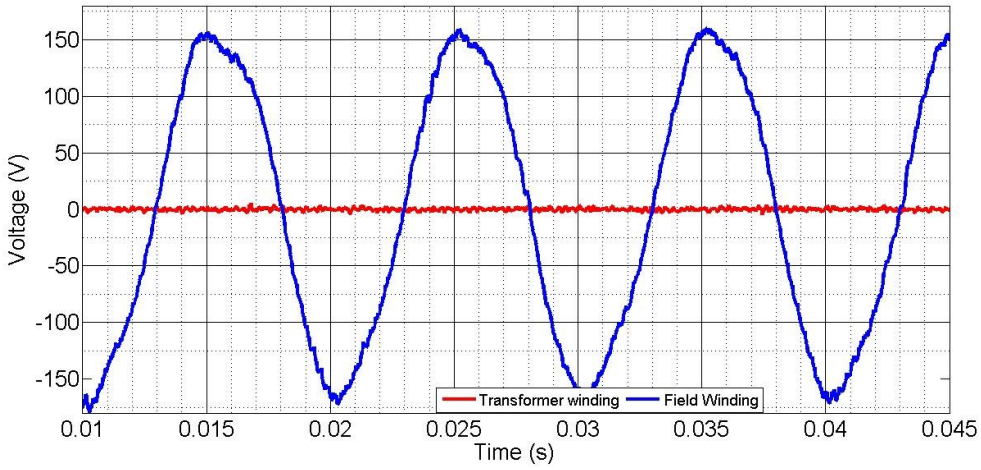

Figure 6.2: Open-circuit test rotor voltages: stator flux aligned with field-winding, experiemental result

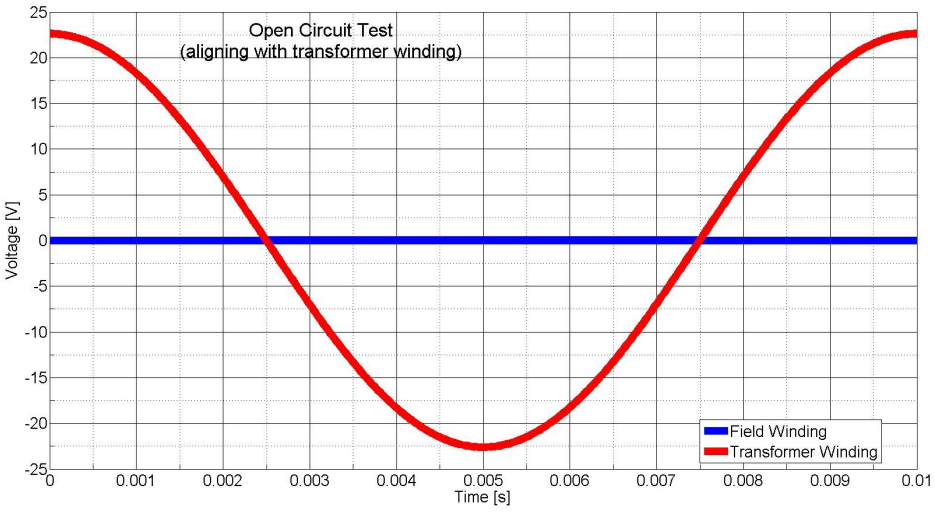

Figure 6.3: Open-circuit test rotor voltages: stator flux aligned with transformer-winding, simulation results

practically decoupled.The simulation and experimental results are reasonably close to each other.This verifies the expected transformer action in both simulation and experiment cases.

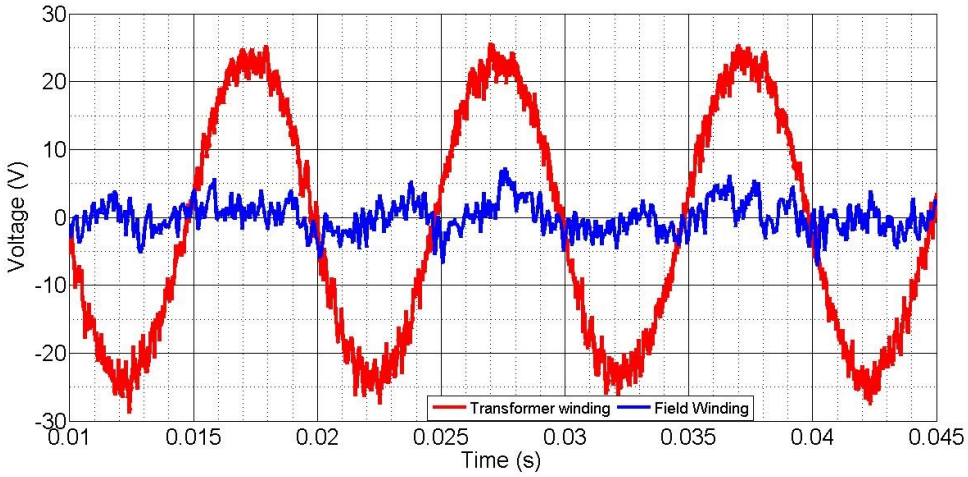

Figure 6.4: Open-circuit test rotor voltages: stator flux aligned with transformer-winding, experimental result

6.2 Locked-Rotor Test

The next test on the prototype machine was the locked-rotor (i.e., zero rotor speed) test. In the case of the locked-rotor test, the objective was to verify the operation of the rectifier, as well as demonstrate torque generation. The fact that the rotor is stationary during the experiment allows us to directly measure the rotor currents and voltages. The rotor is locked at a fixed position, at an angle that maximizes the transformer voltage. Similar to the open-circuit test, a voltage will be induced in the rotor windings from the stator magnetic flux which is generated by the quadrature axis-stator current. The stator flux induces voltage on the transformer winding, which will then be rectified and provide DC current to the field winding.

6.2.1 Simulation

For simulation, the rectifier model of the FEA machine model was enabled, and the rotor position is set at the angle that maximizes the transformer voltage. The test current is then applied. For this particular case, two sets of test cases with carrier currents of 5A and 10A at 150 Hz were applied and fundamental component set to zero. A third case with carrier component of 5A, 150Hz and fundamental component of 15A was also applied evaluate torque production.

6.2.2 Experiment

In the experiment, the locked-rotor test was performed with the rectifier input terminals connected to the transformer winding and the rectifier output terminals connected to the field winding. The rotor is locked to prevent it from spinning as torque is developed when currents are applied to the machine. Similar to the simulation cases, the three test cases are considered.

6.2.3 Results

In the case of the locked-rotor test, as the machine is not spinning, it is possible to measure the current through the transformer and field windings. So, the results include these current and voltage waveforms for the corresponding windings of the rotor. The rotor winding voltage and current values for each winding are plotted comparing the experimental results with that of the simulation on the same figure.

We can see from Figure 6.5 - Figure 6.12 that the current waveforms of the experimental results closely match that of the simulation for the 5A carrier current test. For the test cases with a carrier component of 10A, however, the field current shows a slight mismatch and, for the voltages, the simulation result is higher by up to 20%. During the test, oscillations are observed in the measured rotor voltages.

This disagreement is attributed to modeling errors. There are several known sources of modeling errors which could potentially contribute to the disagreement. For the B-H curve used in the simulation, we have used a simple three-parameter curve for M19 steel from, the accuracy of which is not clear. Because the inductances are large, the inclusion of (reasonably sized) capacitors in the rotor circuit introduces highly underdamped resonant modes in the 100-200Hz frequency range, which broadly overlaps with the operating frequencies investigated in this thesis. Accurately capturing behavior near the resonant frequency is difficult since the highly underdamped behavior results in exaggerated sensitivity to modeling errors. Even if attempts are made to avoid exciting the resonant frequencies directly, there are many mechanisms with which they can be indirectly excited.

Figure 6.13 and Figure 6.14 respectively show the three-phase stator currents for

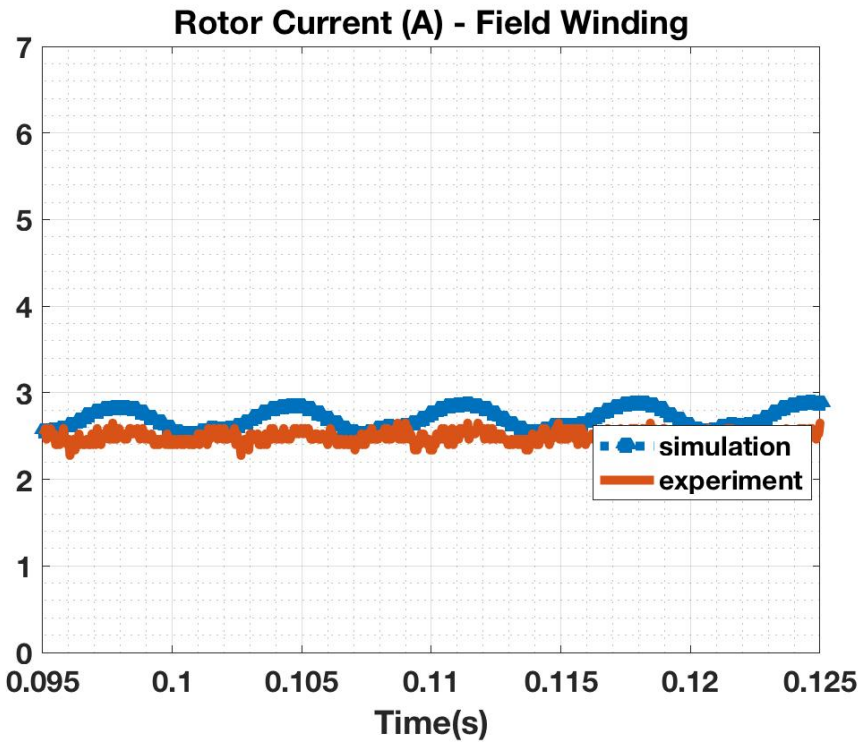

Figure 6.5: Locked-rotor test: simulation and experiment results for field-winding current, test at stator current carrier component of 5A and 150Hz

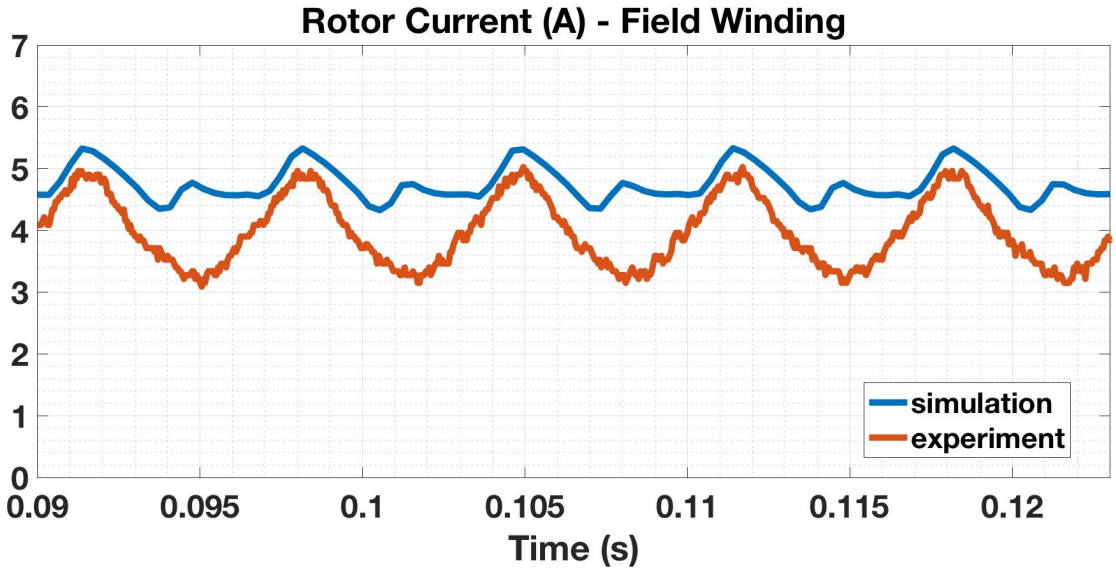

Figure 6.6: Locked-rotor test: simulation and experiment results for field-winding current, test at stator current carrier component of 10A and 150Hz

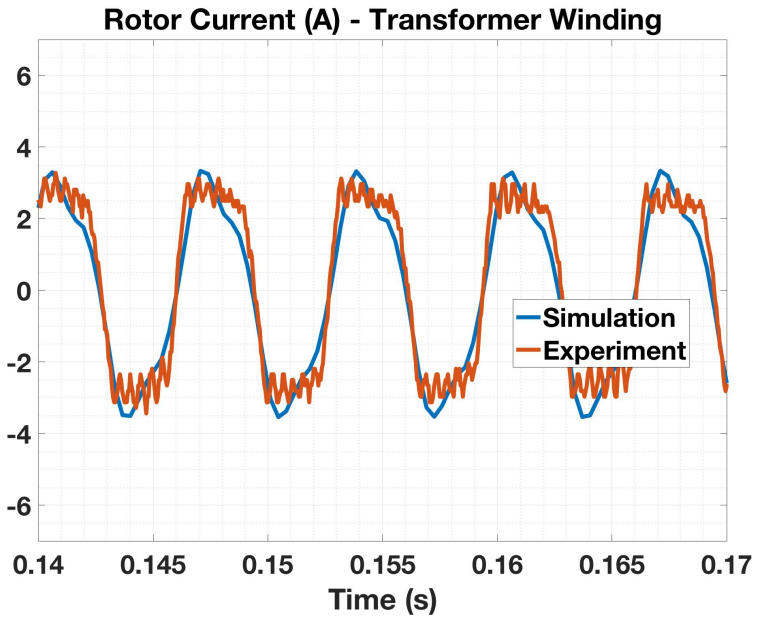

Figure 6.7: Locked-rotor test: simulation and experiment results for transformer-winding current, carrier current at 5A and 150Hz

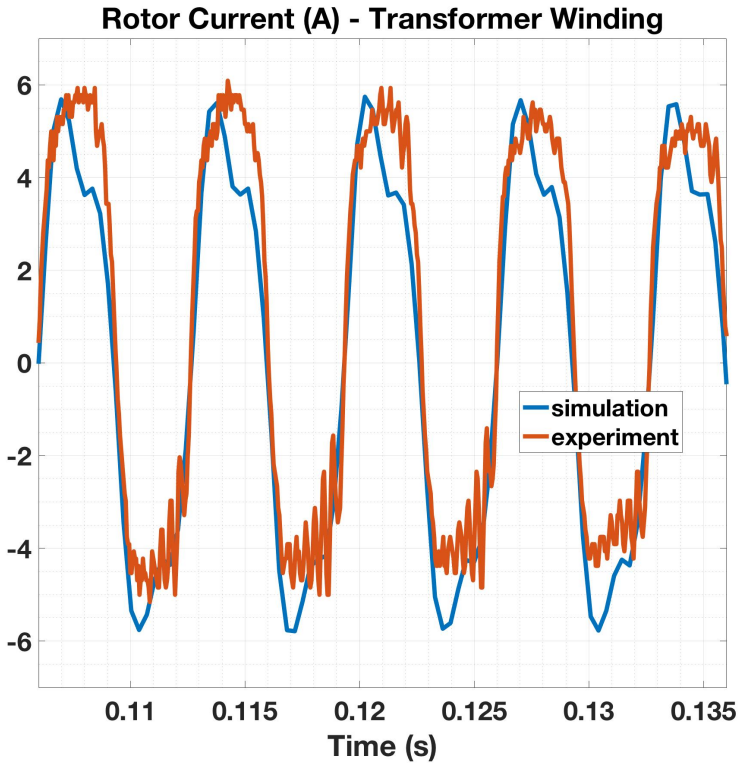

Figure 6.8: Locked-rotor test: simulation and experiment results for transformer-winding current, carrier current at 10A and 150Hz

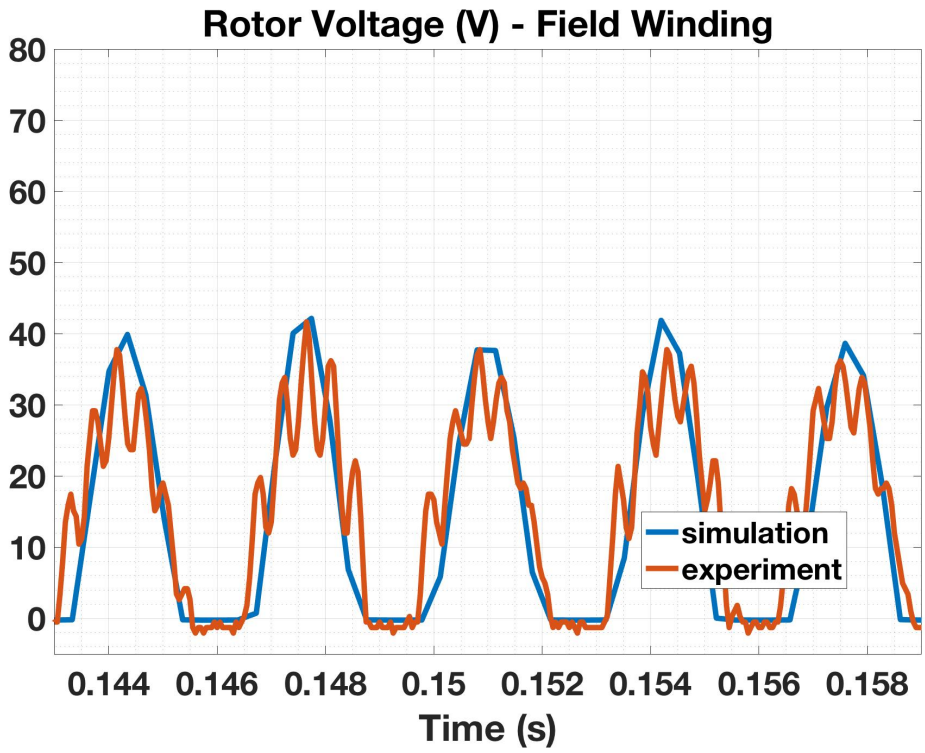

Figure 6.9: Locked-rotor test: simulation and experiment results for field-winding voltage, carrier current at 5A and 150Hz

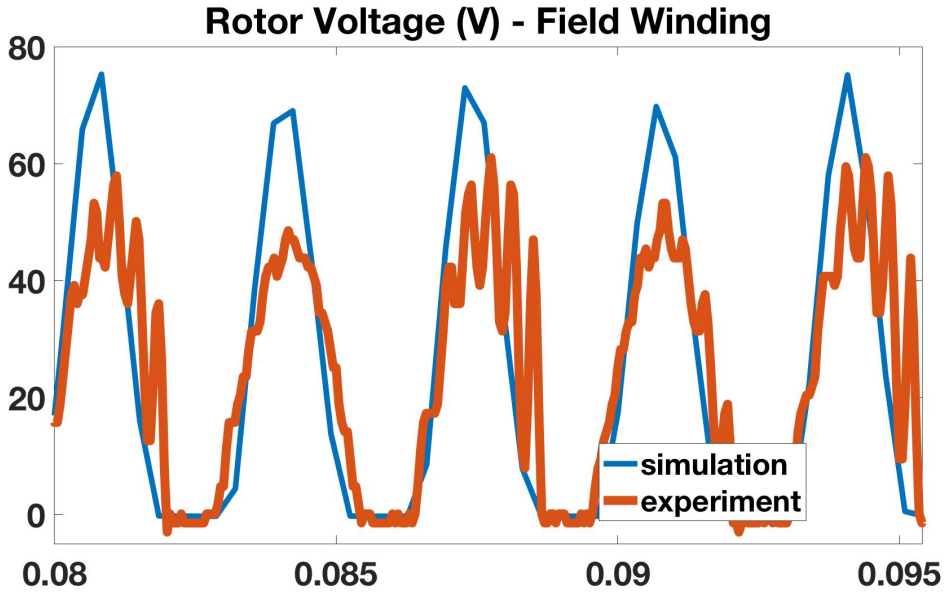

Figure 6.10: Locked-rotor test: simulation and experiment results for field-winding voltage, carrier current at 10A and 150Hz

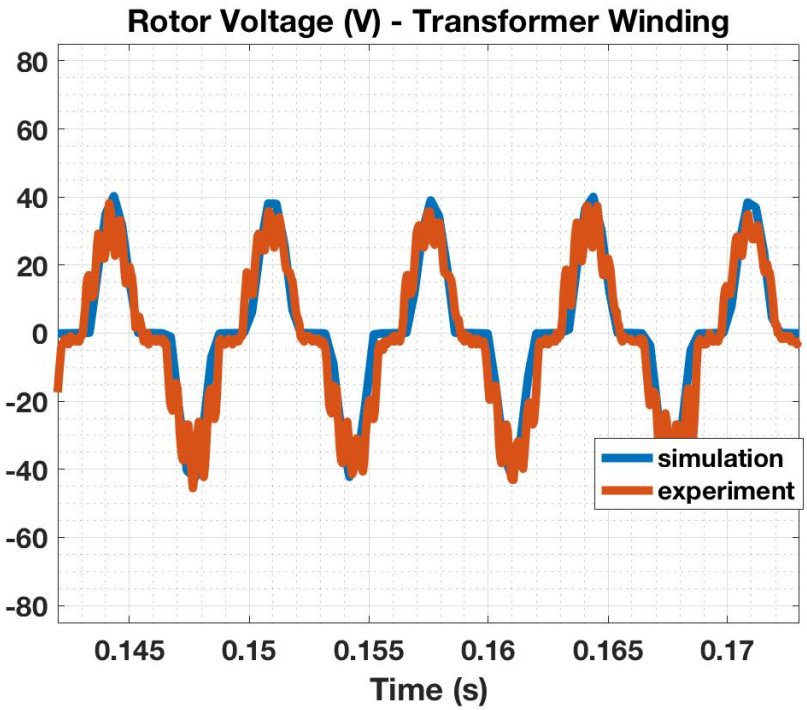

Figure 6.11: Locked-rotor test: simulation and experiment results for transformer-winding voltage, carrier current at 5A and 150Hz

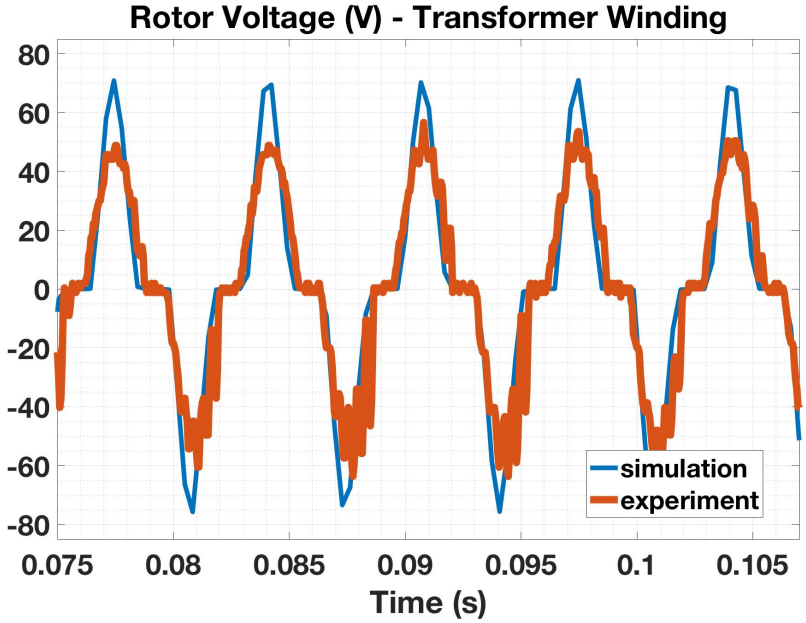

Figure 6.12: Locked-rotor test: simulation and experiment results for field-transformer voltage, carrier current at 10A and 150Hz

simulation and experiment, with the stator quadrature-axis current having a carrier component of magnitude 5A and fundamental component of 10A. As can be seen from the figure, the peak-to-peak value of the current oscillation is as expected.

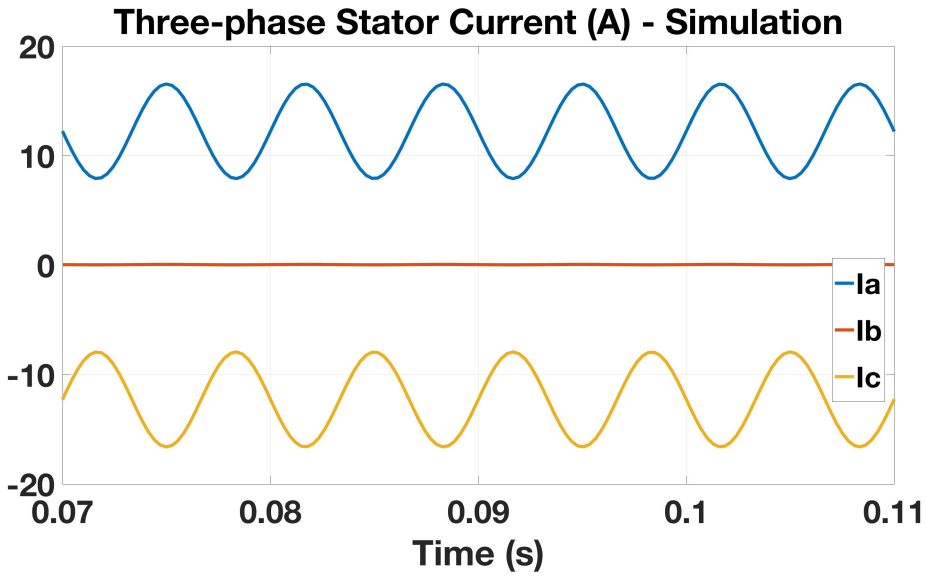

Figure 6.13: Locked-rotor test: prototype machine stator currents, simulation

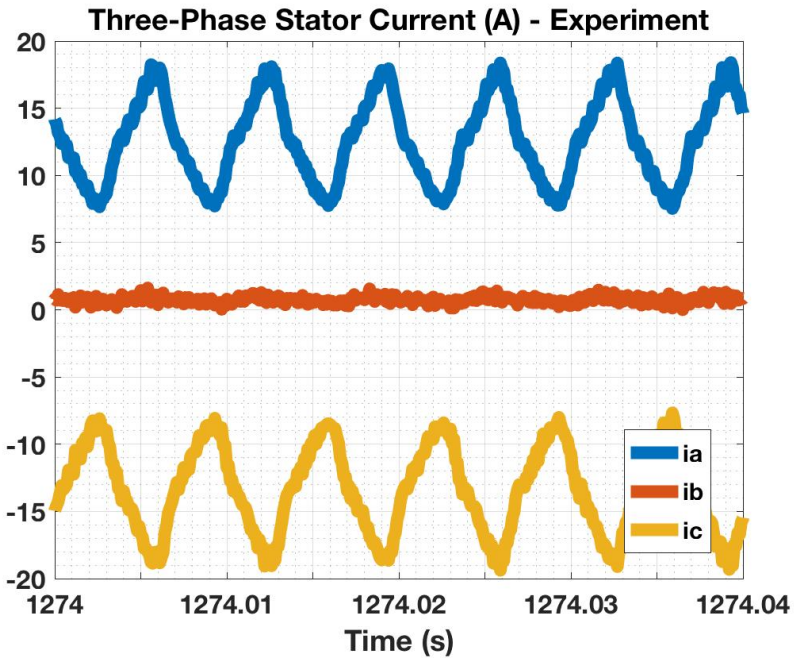

Figure 6.14: Locked-rotor test: prototype machine stator currents, experiment

Figure 6.15 shows the measured and simulated torque under the same test condi-

tion of stator quadrature axis current having a carrier component of magnitude 5A, and fundamental component of 10A.

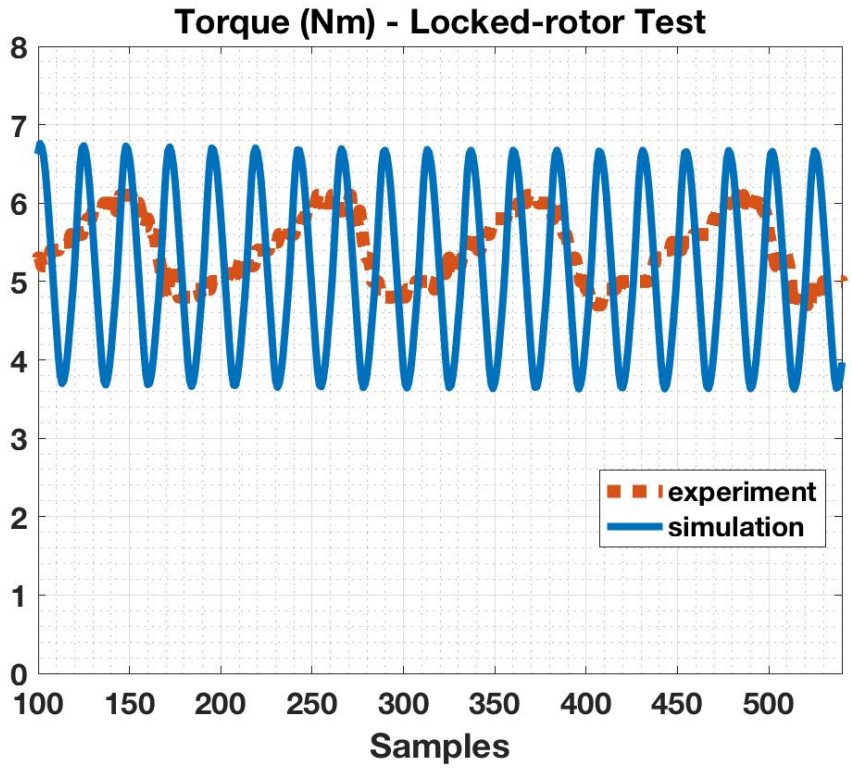

Figure 6.15: Locked-rotor test: simulation and experiment results for torquet, carrier current at 5A, 150Hz and fundamental component of 10A

We can see from the torque plots that the two are closely matching in the average sense. The experimental measurement also exhibits lower torque ripple, which can be attributed to the dampening effect of the inertia of the machine and the coupling in the test setup, and also possibly due to filtering in the torque transducer or possible aliasing effect, as it has a low sampling rate (10 Samples/s).

Overall, the locked-rotor test results agree with expectation and verify the rectifier operation as well as demonstrate torque generation.

6.3 Spin Test

In the case of the spin test, unlike the case of the locked-rotor test, the rotor is allowed to spin. The experimental setup for the prototype machine is as discussed in (§ 5.1). In this test fixture, the induction machine regulates the speed. Once the steady state value of the commanded speed is reached, torque from the prototype machine is applied by changing the fundamental and quadrature components of the quadrature-axis stator current into the prototype machine.

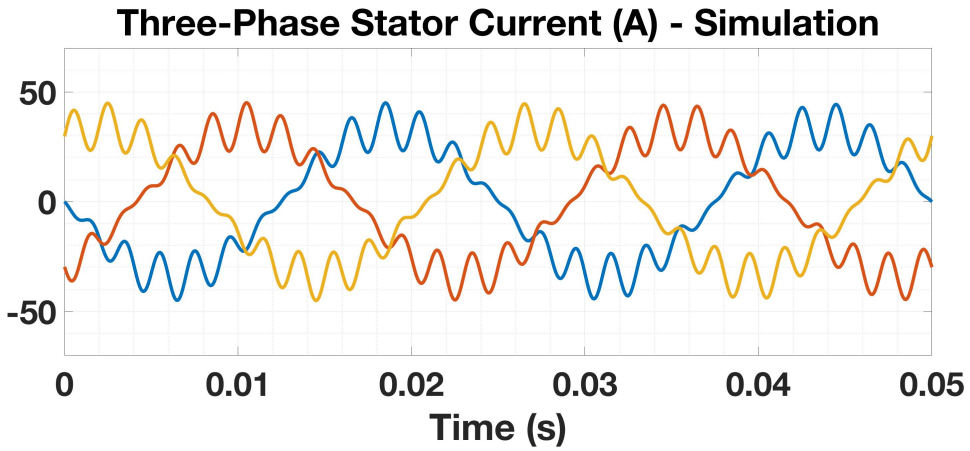

Figure 6.16: Spin test: protorype machine stator currents, simulation

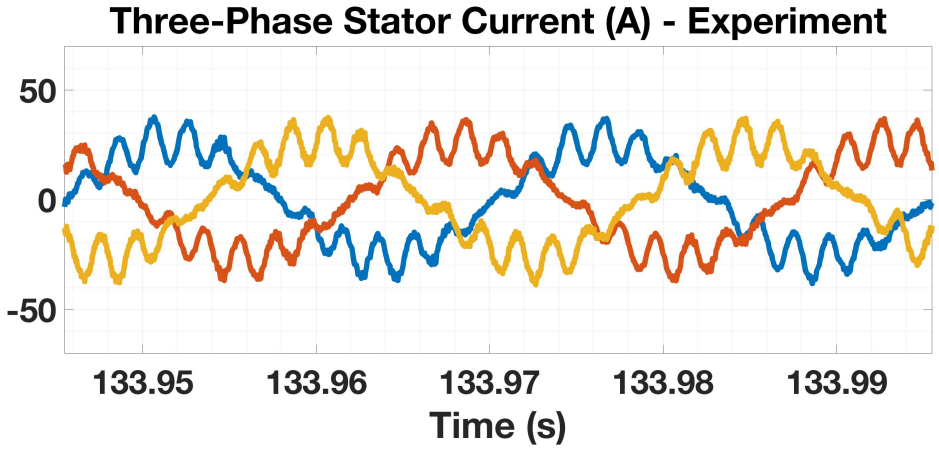

Figure 6.17: Spin test: protorype machine stator currents, experiement

As the rotor is spinning, there is no access to measure the rotor winding voltage

or currents. What can be measured in this case are the stator current waveforms, shaft torque and the three-phase inverter power using the tools and experimental setup discussed in (§ 5.1). Stator current waveforms from the spin test experiment are shown in Figure 6.16 , and the corresponding simulation results are shown in Figure 6.17 . This data was taken while operating at a carrier current of 12A at 500Hz, and 27A fundamental component with the rotor spinnning 1200 rpm. This is consistent with expectations in terms of the modulation behavior observed.

The results presented hereafter focus mainly on the experimental results of the prototype machine in comparison with a benchmark induction machine, which the prototype machine is designed from, both using the same three-phase stator.

In **initial** experiments, the driving induction machine regulated the speed at 2200 rpm and the prototype machine torque is adjusted through the command currents, into the prototype machine. At the time of this experiment, a torque transducer was not available and the output torque of the prototype machine was estimated from the electrical waveforms of the induction machine. From the dynamics of the stator flux-linkage in the stationary reference frame,

$$\frac{d\vec{\lambda}_s}{dt} = \vec{v}_s - R_s\vec{i}_s \tag{6.1}$$

The flux linkage is estimated by

$$\hat{\vec{\lambda}}_s = \int (\vec{v}_s - \hat{R}_s\vec{i}_s)dt, \tag{6.2}$$

The torque was then estimated using the measured current and estimated parameters of the machine.

$$\tau_{est} = \frac{3P}{4}|\hat{\vec{\lambda}}_s|\vec{i_{sq}^{\lambda_s}} \tag{6.3}$$

Figure 6.18 shows the average torque as a function of the quadrature-axis stator current carrier component, while keeping the fundamental component constant at 42A. Figure 6.19 shows the variation of average torque as a function of the quadrature-axis stator current fundamental component, while keeping the carrier component constant at 7A. Two sets of experiment were performed at 250Hz and 5ooHz carrier frequencies. The results are as shown in the figures.

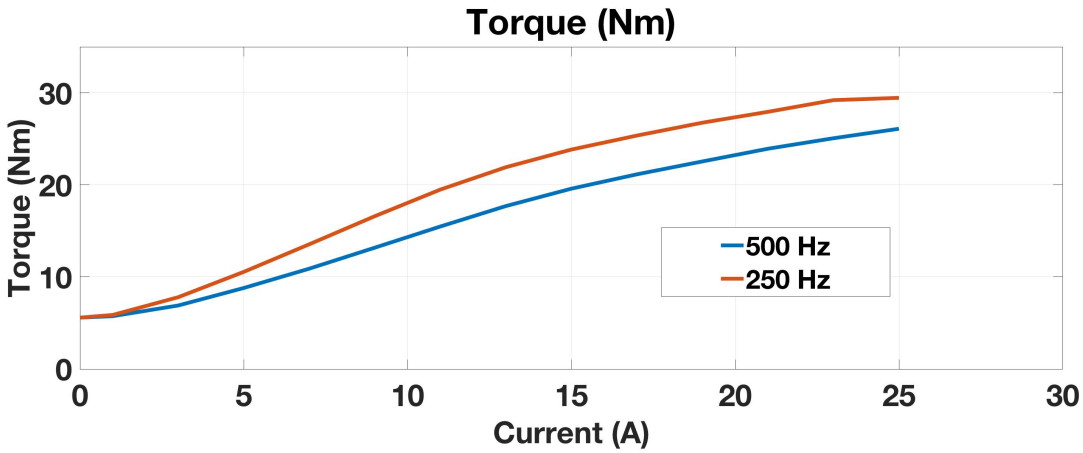

Figure 6.18: Estimated torque as function of carrier component magnitude of the quadrature current, fundamental component at 42A

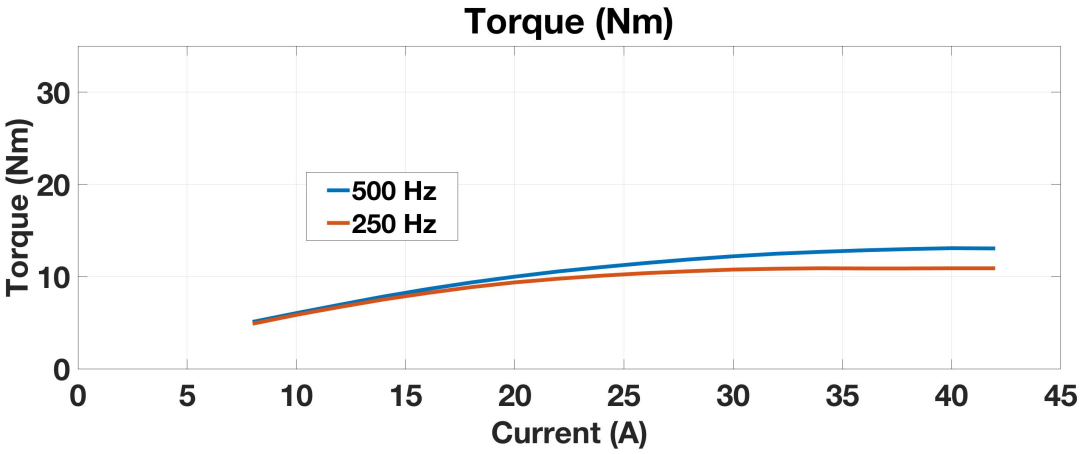

Figure 6.19: Estimated torque as function of fundamental component magnitude of the quadrature current, carrier component at 7A

6.4 Comparing Prototype Machine with Induction Machine

Comparison between the prototype machine and the induction machine based on the initial experiments are shown in Figure 6.20, where estimated output torque is plotted as a function of stator rms current. The magnitudes of the fundamental and carrier frequency components of the stator current were selected to maximize torque output. Two separate tests were conducted on the prototype machine.

These results are compared to those taken on an induction machine which has the same stator as the prototype. The induction machine was operated at the slip frequency corresponding to the Maximum Torque per Amp operating point.

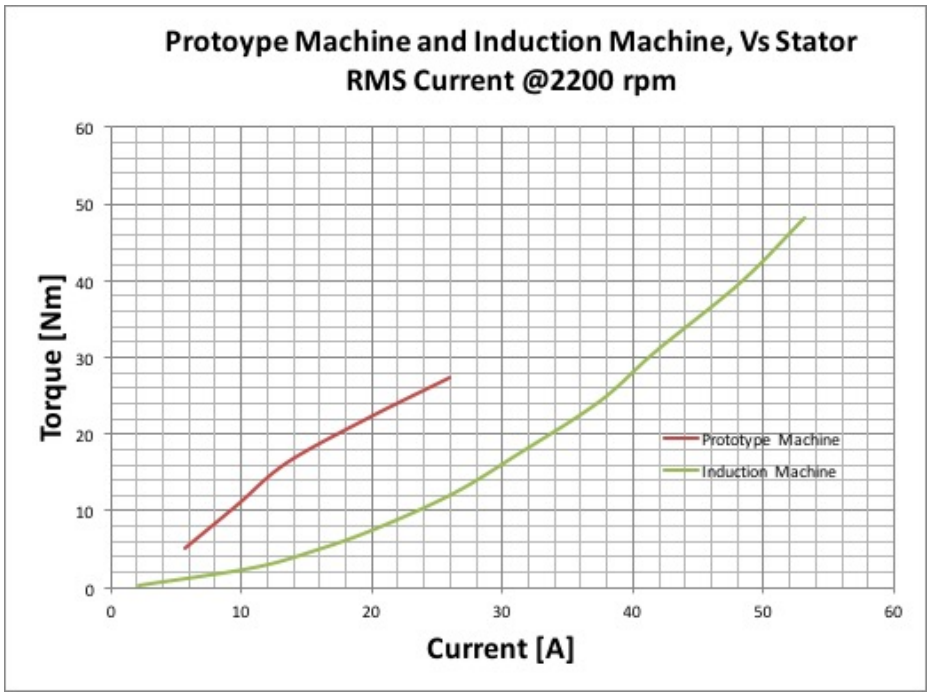

Figure 6.20: Torque vs. rms stator current for prototype and induction machine, estimated torque

6.4.1 Key Observation

These initial results helped to identify limitations on the prototype machine, as it was not posssible to achieve higher torque even if the current command to the

controller was increased. It was originally assumed to be current regulator bandwidth limit due to the frequency of carrier component.

Further experiments and analysis, however, reveal that the issue is from the fact that the prototype machine requires a higher bus voltage to provide the current modulation due to the carrier component. This will create a higher peak value of voltage, even though the RMS value is smaller for a given torque.

Once this was discovered, it was decided to perform the comparison at a lower speed of rotation to reduce overall machine voltages.

For the final experiments, the machines operate at 1200 RPM. This time, a torque transducer was acquired and hence torque is measured instead of estimated as in the previous case. During the experiment, a wide range of possible values for both the fundamental and carrier components of the quadrature-axis were varied, and are shown in the appendix.

Based on the results from these experiments, Figure 6.21 shows torque measured at the maximum torque-per-stator-rms-current operating point for both the prototype and the induction machines. Both test machines were running as generator during the test. From the figure, we can see that the prototype machine has superior torque performance than the induction machine. The efficiency of the prototype machine is also shown to be better in general. Under these operating points, a maximum efficiency of about 86% for the prototype machine is observed delivering power of about 2.1 kW. The maximum efficiency observed in the case of the induction machine is about 78%, delivering power of about 970W. Additional data and performance measurement calculations under this operating condition is given below in Table 6.1 and Table 6.2 for the prototype and the induction machines, respectively.

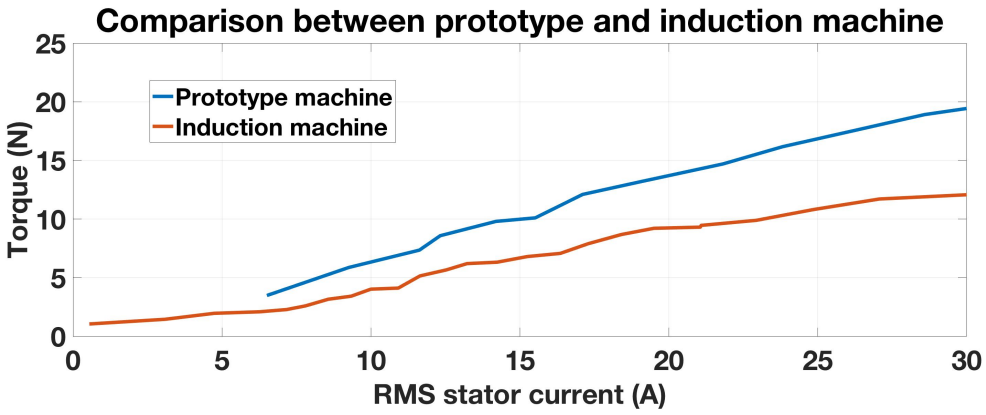

Figure 6.21: Torque vs. RMS stator current for prototype and induction machine, operating to maximize torque per current

Table 6.1: Prototype machine 1200 RPM spin test data - maximum torque per stator rms current operating point

Isrms (A)	Torque (Nm)	Elec.Power (W)	Mech.Power (W)	Efficiency (%)
6.51	3.48	269.00	437.31	61.51
9.26	5.87	587.00	737.65	79.58
11.63	7.35	515.00	924.24	55.72
12.33	8.58	875.00	1078.19	81.15
14.20	9.80	864.00	1231.09	70.18
15.52	10.10	1075.00	1269.52	84.68
17.11	12.10	1156.00	1520.91	76.01
19.08	13.20	1087.00	1658.76	65.53
21.82	14.70	1378.00	1847.56	74.58
23.82	16.17	1288.10	2033.51	63.34
26.49	17.70	1568.40	2224.43	70.51
28.59	18.91	1446.90	2382.64	60.73
30.73	19.70	2123.00	2481.76	85.54
31.12	20.00	1705.80	2512.86	67.88
32.06	22.76	2197.80	2860.11	76.84
42.60	24.60	2424.60	3092.87	78.39

Table 6.2: Induction machine 1200 RPM spin test data - maximum torque per stator rms current operating point

Isrms (A)	Torque (Nm)	Elec.Power (W)	Mech.Power (W)	Efficiency (%)
3.09	1.45	22.47	182.12	12.34
4.74	1.96	66.56	225.80	29.48
6.27	2.09	115.47	262.53	43.98
7.17	2.28	149.57	285.75	52.34
7.80	2.59	179.43	327.04	54.86
8.57	3.16	225.48	399.15	56.49
9.34	3.42	264.66	432.31	61.22
10.00	4.02	310.73	504.33	61.61
10.92	4.11	357.53	519.02	68.89
11.65	5.15	400.86	645.50	62.10
12.53	5.66	478.28	714.52	66.94
13.23	6.20	519.50	777.82	66.79
14.24	6.32	572.68	790.55	72.44
15.25	6.80	626.93	850.74	73.69
16.36	7.07	686.16	884.74	77.55
17.30	7.90	766.34	990.26	77.39
18.41	8.68	812.00	1085.76	74.79
19.50	9.21	836.72	1163.15	71.94
21.06	9.31	921.72	1177.14	78.30
21.09	9.46	921.72	1183.83	77.86
22.94	9.89	968.33	1238.26	78.20
24.86	10.81	1039.00	1353.44	76.77
27.07	11.71	1038.00	1464.65	70.87
33.22	12.47	1076.00	1573.82	68.37
33.39	12.55	1076.00	1571.69	68.46

CHAPTER VII

Conclusion and Summary of Future Work

7.1 Conclusions

7.1.1 FEA Machine Simulation Model

The simulation model result gave significant insight into the operation of the proposed machine. Most of the results match reasonably well with experimental values. However, disagreement between the simulation results and experimental measurements is observed.

There are several known sources of modeling errors which potentially contribute to the disagreement. Firstly, the experiments utilize an existing stator design. In order to incorporate this stator into our simulations, it was necessary to determine the stator tooth and slot dimensions without destroying the stator. This proved difficult, especially when attempting to accurately determine the stator inner diameter. This directly affects the modelled air gap length, which is a key parameter in determining the overall machine inductances. Similarly, nothing is known about the stator B-H curve; we have assumed the material is the same as that used for the rotor laminations. Unfortunately, the only information we have on the rotor lamination B-H curve is the maximum permeability. For the B-H curve used in the simulation, we have used simple three-parameter curve for M19 steel, the accuracy of which is dubious. All of these

geometric and B-H curve errors cumulatively affect the self and mutual inductances of both the stator and rotor windings.

Because the inductances are large, the inclusion of (reasonably sized) capacitors in the rotor circuit introduces highly underdamped resonant modes in the 100-500Hz frequency range, which broadly overlaps with the operating frequencies investigated in this paper. Accurately capturing behavior near the resonant frequency is difficult since the highly underdamped behavior results in exaggerated sensitively to modeling errors. Even if attempts are made to avoid exciting the resonant frequencies directly, there are many mechanisms by which they can be indirectly excited; for example, through mutual inductances, which are often time-varying due to stator-rotor slot interactions and magnetic nonlinearity. Finally, effects like switching harmonics, current regulation error, end-turn and ac winding resistances were not included in the simulation model, all of which contribute to the observed discrepancies. Neglecting the AC winding resistance in particular decreases the damping in the simulation model when compared to the actual machine.

As mentioned above, from earlier experiments, deviation between the simulation results and the measured values were observed. It was originally assumed to be mainly due to modeling errors. Further experiments done recently reveal that the measured values exhibit resonance effects, and selecting the filtering capacitors of the rectifier circuit has a significant efect on the performance. The rotor voltage waveforms in particular were observed to have noticable oscilations due to resonance. With proper selection of the capacitors and the carrier current frequency, performance was improved.

These experiments and simulation also revealed the need for a larger voltage in order to deliver larger power, and hence the machine is limited by the DC bus voltage. This is the reason why the comparison with the benchmark induction machine was performed at a lower speed of 1200 rpm.

7.1.2 Proof-of-Concept and Machine Design

This work accomplished a proof-of-concept for the proposed Self-Excited Synchronous Field-Winding machine design topology. Torques close to 25 Nm were developed at 1200 rpm. The comparison with a benchmark induction machine proved that the proposed prototype machine has superior performance in terms of torque as well as improved efficiency for a given RMS stator current, operating in maximum-torque-per-stator-rms-current operating point.

7.2 Future Work

Experimental results shown that the prototype machine possesses a superior torque-per-amp performance when compared with the induction machine, under the operating point described. However, some difficulties were encountered when trying to achieve higher torque levels. The described limit on the DC bus voltage is a major one, as well as failure modes in the rectifier circuit of the rotor design, particularly observed in the capacitors, is another. Future work to resolve these observed issues are as follows:

7.2.1 Rotor Rectifier Circuit Failure Mode

The rotor winding voltages are observed to reach a level larger than the voltage rating of the capacitors when the stator current carrier magnitude is increased to 35A or above. In addition, the resonance effects were observed to generate large voltages, depending on the carrier frequency, and the capacitor values used the failure mode.

A mechanism to limit the voltage reacing the capacitors and optimizing the resonance performance can improve the performance more.

7.2.2 DC Bus Voltage Constraint Performance

The experiments were conducted using the same stator designed for the induction machine. Optimizing the rotor windings design could help lower the level of voltage required from the DC bus for a given power. This rotor winding optimization will also help with the failure mode mentioned above.

7.2.3 Control algorithm

The control strategy used in the experiments consists of standard FOC with the addition of carrier current component in the quadrature axis current command. An

optimal control strategy to determining the command carrier and fundamental component, for different operating points will be another future work to consider. This will enable improved performance in variable-speed applications, and also help in the complete characterization of the machine.

APPENDICES

APPENDIX A

Prototype Machine Experimental Data

Tables below give the complete data collected during the experiment on the prototype machine for a range of values maping the attainable stator current quadrature axis fundamental and carrier components. The experiment is performed on a DC bus voltage of 280V and rotor spinning at 1200 rpm. The same experimental setup is used here the prototype operating as generator.

Table A.1: Prototype machine 1200 RPM spin test data - commanding carrier current magnitude of 5A, and frequency 150 Hz, while varying the fundamental current command

Isq Fundamental (A)	Isq RMS (A)	Torque Measured (Nm)	Elec.Power Measured (W)	Mech.Power (Speed x Torque) (W)	Efficiency (%)
5	4.43	1.96	213	246.26	86.49
10	7.63	3.57	437	448.17	97.51
15	11.02	5.32	619	668.48	92.6
20	14.49	5.87	703	737.03	95.38
25	17.99	5.85	683	735.5	92.86
30	21.48	5.28	610	662.29	92.1
35	24.98	4.69	511	589.26	86.72
40	28.46	4.03	427	506.76	84.26
45	31.98	4.06	345	510.02	67.64
50	35.51	3.79	264	476.46	55.41
55	39.02	3.36	180	421.98	42.66
60	42.54	3.65	96.8	458.56	21.11
65	46.06	3.62	9.43	455.21	2.07

Table A.2: Prototype machine 1200 RPM spin test data - commanding carrier current magnitude of 10A, and frequency 150 Hz, while varying the fundamental current command

Isq Fundamental (A)	Isq RMS (A)	Torque Measured (Nm)	Elec.Power Measured (W)	Mech.Power (Speed x Torque) (W)	Efficiency (%)
5	6.51	3.48	269	437.31	61.51
10	9.26	5.87	587	737.65	79.58
15	12.33	8.58	875	1078.19	81.15
20	15.52	10.1	1075	1269.52	84.68
25	18.83	10.5	1160	1320.24	87.86
30	22.17	10.5	1145	1318.92	86.81
35	25.57	9.64	1053	1211.3	86.93
40	29.4	10.1	1153	1267.09	91
45	32.38	9.39	980	1179.39	83.09
50	35.86	7.8	736	979.52	75.14
55	39.35	6.5	530	816.61	64.9
60	42.84	5.64	343	709.75	48.33
65	46.33	5.02	183	630.78	29.01

Table A.3: Prototype machine 1200 RPM spin test data - commanding carrier current magnitude of 15A, and frequency 150 Hz, while varying the fundamental current command

Isq Fundamental (A)	Isq RMS (A)	Torque Measured (Nm)	Elec.Power Measured (W)	Mech.Power (Speed x Torque) (W)	Efficiency (%)
5	9.6	4.42	147	555.71	26.45
10	11.63	7.35	515	924.24	55.72
15	14.2	9.8	864	1231.09	70.18
20	17.11	12.1	1156	1520.91	76.01
25	20.14	13.4	1358	1684.45	80.62
30	23.28	13.7	1434	1721.31	83.31
35	26.5	13.2	1407	1657.52	84.89
40	29.66	15.7	1704	1973.41	86.35
45	33.04	15.1	1599	1899.74	84.17
50	36.43	13.9	1410	1746.87	80.72
55	39.86	10.7	1059	1344.94	78.74
60	43.3	9.47	771	1191.62	64.7
65	46.76	7.96	505	999.87	50.51

Table A.4: Prototype machine 1200 RPM spin test data - commanding carrier current magnitude of 20A, and frequency 150 Hz, while varying the fundamental current command

Isq Fundamental (A)	Isq RMS (A)	Torque Measured (Nm)	Elec.Power Measured (W)	Mech.Power (Speed x Torque) (W)	Efficiency (%)
5	13.27	4.67	120	586.85	20.45
10	14.7	7.8	316	980.5	32.23
15	16.65	10.6	727	1331.7	54.59
20	19.08	13.2	1087	1658.76	65.53
25	21.82	14.7	1378	1847.56	74.58
30	24.71	16	1571	2009.45	78.18
35	27.75	16	1632	2011.46	81.14
40	30.73	19.7	2123	2481.76	85.54
45	33.94	19.3	2024	2426.32	83.42
50	37.21	18	1760	2266.85	77.64
55	40.57	16.6	1655	2087.93	79.27
60	43.94	14	1299	1757.83	73.9
65	47.35	11.3	940	1417.99	66.29

Table A.5: Prototype machine 1200 RPM spin test data - commanding carrier current magnitude of 25A, and frequency 150 Hz, while varying the fundamental current command

Isq Fundamental (A)	Isq RMS (A)	Torque Measured (Nm)	Elec.Power Measured (W)	Mech.Power (Speed x Torque) (W)	Efficiency (%)
25	23.82	16.17	1288.1	2033.51	63.34
30	26.49	17.7	1568.4	2224.43	70.51
35	29.25	18.38	1746.2	2307.97	75.66
40	32.06	22.76	2197.8	2860.11	76.84
45	35.11	22.38	2390.8	2808.84	85.12
50	38.26	21.74	2251.8	2731.93	82.43
55	41.47	20.95	2073.4	2632.44	78.76
60	44.76	18.76	1793.8	2360.2	76
65	48.08	15.9	1421.3	2000.88	71.03

Table A.6: Prototype machine 1200 RPM spin test data - commanding carrier current magnitude of 30A, and frequency 150 Hz, while varying the fundamental current command

Isq Fundamental (A)	Isq RMS (A)	Torque Measured (Nm)	Elec.Power Measured (W)	Mech.Power (Speed x Torque) (W)	Efficiency (%)
25	26.26	16.36	1091.5	2055	53.11
30	28.59	18.91	1446.9	2382.64	60.73
35	31.12	20	1705.8	2512.86	67.88
55	42.6	24.6	2424.6	3092.87	78.39
60	45.77	22.71	2170.6	2858.1	75.95
65	49.01	20.11	1851.3	2524.57	73.33

Table A.7: Prototype machine 1200 RPM spin test data - commanding carrier current magnitude of 35A, and frequency 150 Hz, while varying the fundamental current command

Isq Fundamental (A)	Isq RMS (A)	Torque Measured (Nm)	Elec.Power Measured (W)	Mech.Power (Speed x Torque) (W)	Efficiency (%)
30	29.75	19.2	1353.8	2414.55	56.07
35	28.24	21.69	1548.6	2727.24	56.78
65	50.05	23.87	2202.2	3005.34	73.28

Bibliography

[1] James R. Melcher. *Continuum Electromechanics*. Number 1. The MIT Press; First Edition, First Printing edition, 1981.

[2] R.W. de Doncker A. Veltman, D.W.J. Pulle. Springer, 2008.

[3] A.K. Adnanes, R. Nilssen, and R.O. Rad. Power feed-back during controller failure in inverter fed permanent magnet synchronous motor drives with flux weakening. In *Power Electronics Specialists Conference, 1992. PESC '92 Record., 23rd Annual IEEE*, pages 958–963 vol.2, Jun 1992.

[4] A.E. Fitzgerald, Charles Kingsley, Jr., Stephen D. Umans. *Electric Machinery*. Number 5. McGra-Hill, Inc., 1990.

[5] P Albertos and a. Sala. *Multivariable Control Systems*. 2004.

[6] G. F. H. Allen. Brushless excitation systems for synchronous machines. *Electronics and Power*, 21(15):866–869, September 1975.

[7] Eleanor Bash. *Recent Development of Electrical Drives*, volume 1. 2015.

[8] Tang Danlu. Rare earth prices to remain strong, 2011. [Online; accessed 12-January-2014].

[9] Bill Drury. *Control Techniques Drives and Controls Handbook (2nd Edition)*. Institution of Engineering and Technology, 2001.

[10] A.M. EL-Refaie and T.M. Jahns. Comparison of synchronous pm machine types for wide constant-power speed range operation. In *Industry Applications Conference, 2005. Fourtieth IAS Annual Meeting. Conference Record of the 2005*, volume 2, pages 1015–1022 Vol. 2, Oct 2005.

[11] E.D. Ganev. High-performance electric drives for aerospace more electric architectures part i – electric machines. In *Power Engineering Society General Meeting, 2007. IEEE*, pages 1–8, June 2007.

[12] Jacek F. Gieras. *Advancements in Electric Machines*. Springer, 2008.

[13] W. Gruber, T. Hinterdorfer, H. Sima, A. Schulz, and J. Wassermann. Comparison of different motor-generator sets for long term storage flywheels. *2014 International Symposium on Power Electronics, Electrical Drives, Automation and Motion, SPEEDAM 2014*, pages 161–166, 2014.

[14] Ron Colyer H. Bulent Ertan, M. Yildirim Uctug and Alfio Consoli, editors. *Modern electric Drives*. Springer, nato asi s edition, 2000.

[15] K.H. Harib, E.A. Khousa, and A. Ismail. Field Oriented Motion Control of a 3-Phase Permanent Magnet Synchronous Motor. *2011 2nd International Conference on Electric Power and Energy Conversion Systems (EPECS)*, 17555:1 – 7, 2011.

[16] Rutuja S. Hiware and J.G. Chaudhari. Indirect Field Oriented Control for Induction Motor. *2011 Fourth International Conference on Emerging Trends in Engineering & Technology*, pages 191–194, 2011.

[17] H. F. Hofmann. High-speed synchronous reluctance machine for flywheel applications, 1998.

[18] Heath Hofmann. *Electric Machinery and Drives (Book draft to be published/ EECS 419 lecture notes, University of Michigan)*.

[19] J. Hur and I. Suzuki. High Rare-Earth Prices Force Hitachi, Toyota to Find Alternative, 2011. [Online; accessed 12-January-2014].

[20] K. Inoue, H. Yamashita, E. Nakamae, and T. Fujikawa. A brushless self-exciting three-phase synchronous generator utilizing the 5th-space harmonic component of magneto motive force through armature currents. *Energy Conversion, IEEE Transactions on*, 7(3):517–524, Sep 1992.

[21] T.M. Jahns. Flux-weakening regime operation of an interior permanent-magnet synchronous motor drive. *Industry Applications, IEEE Transactions on*, IA-23(4):681–689, July 1987.

[22] Joseph P John, S. Suresh Kumar, and B. Jaya. Space Vector Modulation based Field Oriented Control scheme for Brushless DC motors. *2011 International Conference on Emerging Trends in Electrical and Computer Technology*, pages 346–351, 2011.

[23] A. Lebsir, A. Bentounsi, R. Rebbah, S. Belakehal, and M. E H Benbouzid. Comparative study of PMSM and SRM capabilities. *International Conference on Power Engineering, Energy and Electrical Drives*, (May):760–763, 2013.

[24] James Goss-Mircea Popescu Motor Design Ltd Malcolm Burwell-International Copper Association. Performance/cost comparison of induction-motor and permanent-magnet-motor in a hybrid electric car. *International Copper Association, Copper Alliance*, 2013.

[25] Nicola Bianchi. *Elecrrical Machine Analysis Using Finite Elements*. Kluwer Academic Publishers, 1995.

[26] S. Nonaka. A new brushless excitation method for 4-pole three-phase synchronous generator with cylindrical-rotor. In *Industry Applications Society Annual Meeting, 1994., Conference Record of the 1994 IEEE*, pages 23–30 vol.1, Oct 1994.

[27] S. Nonaka and T. Kawaguchi. A new variable-speed ac generator system using brushless self-excited type synchronous machine. In *Industry Applications Society Annual Meeting, 1990., Conference Record of the 1990 IEEE*, pages 691–696 vol.1, Oct 1990.

[28] S. Nonaka and T. Kawaguchi. Excitation scheme of brushless self-excited-type three-phase synchronous machine. *Industry Applications, IEEE Transactions on*, 28(6):1322–1329, Nov 1992.

[29] S. Nonaka and K. Kesamaru. Analysis of voltage-adjustable brushless synchronous generator without exciter. *Industry Applications, IEEE Transactions on*, 25(1):126–132, Jan 1989.

[30] Jason Pries. *Computationally Efficient SteadyState Simulation Algorithms for FiniteElement Models of Electric Machines*. PhD thesis, University of Michigan, 2015. PhD dissertation.

[31] Nannapaneni Narayana Rao. *Fundamentals of electromagnetics for electrical and computer engineering*. Prentice Hall, 2009.

[32] Dragan Maksimovic Robert W. Erickson. *Fundamentals of Power Electronics 2nd Edition (2nd Edition)*. Kluwer Academic Publisher, 2004.

[33] Alexander J Rovnan and Heath F Hofmann. Brushless , Self-Excited Synchronous Field- Winding Machine for Variable-Speed Drive Applications. (702):1–6, 2006.

[34] Sheppard Salon. *Finite Element Analysis of Electrical Machines*. Kluwer Academic Publishers, 1995.

[35] H. Sira-Ramirez, F. Gonzalez-Montanez, J.A. Cortes-Romero, and A. Luviano-Juarez. A Robust Linear Field-Oriented Voltage Control for the Induction Motor: Experimental Results. *IEEE Transactions on Industrial Electronics*, 60(8):3025–3033, 2013.

[36] W.L. Soong and T.J.E. Miller. Field-weakening performance of brushless synchronous ac motor drives. *Electric Power Applications, IEE Proceedings* -, 141(6):331–340, Nov 1994.

[37] Lizhi Sun, Xiaolong Gao, Fei Yao, Quntao An, and T. Lipo. A new type of harmonic current excited brushless synchronous machine based on an open winding pattern. In *Energy Conversion Congress and Exposition (ECCE), 2014 IEEE*, pages 2366–2373, Sept 2014.

[38] Tiecheng Sun, Jingwei Han, Deyan Gao, Sanling Xu, and Ningbo Lu. Research on Field Oriented Control System of Induction Motor Based on Computer. (1):1389–1393, 2012.

[39] T.J.E. Miller. *Brushless Permanent-Magnet and Reluctance Motor Drives*. Number 21. Oxford Science Publications, 1989.

[40] Q V. http://www.valco.eu/articolo/196/electric-motors-high-efficiency/motor-parts—stators–rotors-and-shaft/stator-with-winding-and-rotor-with-shaft.aspx. Accessed: 2017-09-12.

[41] Joseph Vithayathil. Ac machine system with induced dc field checking, us pattent no. us 5,012,148; date filed 09-14-1998, filing no. 407,211.

[42] Joseph Vithayathil. Ac machine system with induced dc field checking, us pattent no. us 6,051,953; date filed 07-24-1998, filing no. 09/122,005, 04 2000.

[43] Slobodan N. Vukosavic. *Digital Control of Electrical Drives*. 2007.

[44] UK W L Soong, D A Staton, T J E Miller, Glasgow University. Validation of Lumped-Circuit and Finite-Element Modelling of Axially-Laminated Brushless Motors. pages 85–90.

[45] Piotr Wach. *Dynamics and Control of Electrical Drives*. Springer, 2011.